

## Simplified method for simulation of incompressible viscous flows inspired by the lattice Boltzmann method

Jun-Jie Huang \*

Department of Engineering Mechanics, College of Aerospace Engineering, Chongqing University, Chongqing 400044, China  
and Chongqing Key Laboratory of Heterogeneous Material Mechanics, Chongqing University, Chongqing 400044, China



(Received 7 December 2020; revised 31 March 2021; accepted 7 May 2021; published 25 May 2021)

The lattice Boltzmann method (LBM) has gained increasing popularity in incompressible viscous flow simulations, but it uses many distribution functions (far more than the flow variables) and is often memory demanding. This disadvantage was overcome by a recent approach that solves the *more actual macroscopic equations* obtained through Taylor series expansion analysis of the lattice Boltzmann equations [Lu *et al.*, *J. Comput. Phys.* **415**, 109546 (2020)]. The key is to keep some small additional terms (SATs) to stabilize the numerical solution of the weakly compressible Navier-Stokes equations. However, there are many SATs that complicate the implementation of their method. Based on some analyses and numerous tests, we ultimately pinpoint two essential ingredients for stable simulations: (1) suitable density (pressure) diffusion added to the continuity equation and (2) proper numerical dissipation related to the velocity divergence added to the momentum equations. Then we propose a simplified method that is not only easier to implement but noticeably faster than the original method and the LBM. It contains much simpler SATs that *only* involve the density (pressure) derivatives, and it requires no intermediate steps or variables. As well, it is extended for thermal flows with small temperature variations and for two-phase flows with uniform density and viscosity. Several test cases, including some two-phase problems under two-dimensional, axisymmetric, and three-dimensional geometries, are presented to demonstrate its capability. This work may help pave the way for the simplest simulation of incompressible viscous flows on collocated grids based on the artificial compressibility methodology.

DOI: [10.1103/PhysRevE.103.053311](https://doi.org/10.1103/PhysRevE.103.053311)

### I. INTRODUCTION

An important and essential step in the numerical simulation of incompressible viscous flows is to find the pressure field, often by the solution of a Poisson equation [1]. It is well known that this step is rather time consuming and makes parallel computing more difficult. Over the past few decades, the lattice Boltzmann method (LBM) has become popular for incompressible flow simulation as it does not need to solve the Poisson equation [2]. LBM may be viewed as one type of artificial compressibility method (ACM) [3–5] because the flow simulated by LBM is actually weakly compressible and the incompressibility condition is just approximately satisfied when the Mach number ( $Ma$ ) is low enough. Due to its explicit nature, LBM is relatively easy to implement and parallelize. However, because of its kinetic origin, LBM has to use many particle distribution functions (PDFs), much more than the number of macroscopic variables, thus consuming more memory resources. From certain perspective, LBM can be considered as a special finite difference method to solve the incompressible Navier-Stokes equations (NSEs) [6,7]. However, the analyses in Refs. [6,7] involved the moments of the PDFs and the scheme proposed in Ref. [6] used semi-implicit temporal discretization (still need to solve an elliptic problem). Is it possible to circumvent the PDFs

and the related moments and directly evolve the weakly compressible NSEs explicitly? The answer has been given recently in Ref. [8], which proposed an alternative method constructed upon the *more actual macroscopic equations* (MAMEs) found by Taylor series expansion analysis of the lattice Boltzmann equations (LBEs). It was shown that direct discretization of the weakly compressible NSEs obtained by the usual Chapman-Enskog analysis are not stable; in contrast, the MAMEs contain small additional terms (SATs) pivotal to stabilize the simulation [8]. The SATs in the MAMEs are rather complex because they contain many terms involving the density (pressure), different velocity components and their derivatives in both space and time. The numerical solution of the MAMEs introduces intermediate variables and uses a predictor-corrector procedure. Besides, proper boundary conditions must be supplied for some additional derivatives (which are not present in the original NSEs). One may be curious on whether the MAMEs can be simplified with some nonessential terms discarded. In this paper, we demonstrate that this can indeed be realized.

By making full use of the low- $Ma$  characteristics of the LBM, we further simplify the temporally discretized equations by discarding some terms of  $O(Ma^2)$  and keeping only derivatives of the density (pressure). Our method is based on the observation that the additional terms are already small and vanish as the time step  $\delta_t \rightarrow 0$  (that is why the MAMEs can converge to the incompressible NSEs). The essential role of the SATs is to stabilize the computation. There may be some

\*jjhuang1980@gmail.com; jjhuang@cqu.edu.cn

room to adjust them as long as their magnitude is maintained at the same order without compromising the simulation (i.e., the stabilizing effects are still kept). From the design point of view, one tends to make them as simple as possible and this can be optimally achieved by leaving *only one scalar variable*. For incompressible flows, the pressure is the only choice (note that in ACM the pressure is tied to the density through an equation of state). Numerical tests indeed showed that under many situations it suffices to just keep the pressure terms. Such simplifications make the method much easier to implement: the predictor and corrector steps in Ref. [8] are now combined into one single step and the intermediate variables are no longer necessary. The issue of boundary conditions for additional derivatives is resolved at the same time. As a result, the simulation needs even less memory and runs even faster. The proposed simplified method is verified through several canonical tests for single-phase flows. What is more, its effectiveness is also proven for thermal flows with Boussinesq approximation (coupled with the heat conduction equation) and for two-phase flows with uniform density and viscosity (coupled with a phase field modeling of the interface dynamics).

In addition to the LBM, there are some other approaches for incompressible flow simulations based on the idea of AC, for instance, the kinetically reduced local Navier-Stokes (KRLNS) [9–11], the ACM with added dissipation [4] (denoted as *suppressing checkerboard instability* (SCI) in Ref. [12]), the linkwise ACM [13], the methods of the entropically damped form of artificial compressibility (EDAC) [14], and the general pressure equation (GPE) [12]. The KRLNS uses a grand potential in the governing equations with an important term missing. It was later corrected by the EDAC which abandons the grand potential and uses common thermodynamic variables [14]. The governing equations in the EDAC method resemble the compressible NSEs except that the continuity equation for the density is replaced by an evolution equation for the pressure containing dissipative terms and the bulk viscosity component is neglected in the viscous stress tensor [14]. In actual implementation, the EDAC method usually employs a *collocated* grid and various schemes can be used for spatial and temporal discretizations, for instance, the second-order MacCormack scheme using a predictor-corrector sequence and the second-order central scheme with high-order Runge-Kutta (RK) schemes for time marching [14–16]. The GPE method is quite similar to the EDAC method in terms of the governing equations, but it uses a *staggered* grid. For time marching, the third-order RK schemes are commonly used for GPE-based simulations [12,17,18]. In general, its implementation is more complicated than those on collocated grids and the simulation speed is slower than other one- or two-step methods. The second-order version of the ACM with added dissipation also uses a *collocated* grid

and intermediate variables for the pressure and velocity [4], thus it may be viewed as a two-step method. The link-wise ACM resembles the LBM to a significant degree, but it may circumvent the use of the PDFs [13]. It also uses a *collocated* grid and is a one-step method. However, the optimized implementation of the linkwise ACM without any PDFs involves many formulas that are quite complicated, especially in three dimensions. Within the general ACM framework, the present method seems to be the simplest and easiest to implement: it uses a collocated grid, the second-order schemes to discretize the spatial derivatives, and one-step time marching.

This paper is organized as follows. Section II first introduces the MAMEs, its relation with the LBEs, and then presents the simplified MAMEs and its implementation. Next, the extension to thermal and two-phase flows is briefly described. Section III provides the study of several common validation cases, including both single- and two-phase problems, by the proposed method and compares the numerical results with other reference ones. Section IV concludes this paper with discussion on future work.

## II. NUMERICAL MODEL AND METHODS

In this part, we first briefly review the LBEs and the MAMEs, and then describe how to obtain the simplified formulation of the MAMEs by analyzing the order of magnitude and using the known macroscopic equations. After that, we introduce its extension to thermal and two-phase problems through the coupling with additional evolution equations for the temperature and the order parameter. Last, we make some comparisons with some other methods in detail.

### A. LBEs and MAMEs

The standard LBEs using single relaxation time read

$$f_i(\mathbf{x} + \mathbf{e}_i \delta_t, t + \delta_t) - f_i(\mathbf{x}, t) = -\frac{1}{\tau_f} [f_i(\mathbf{x}, t) - f_i^{eq}(\mathbf{x}, t)], \quad (1)$$

where  $\mathbf{e}_i = c(k_x \mathbf{e}_x + k_y \mathbf{e}_y + k_z \mathbf{e}_z)$  is the discrete velocity ( $c$  is the magnitude of lattice velocity,  $k_x$ ,  $k_y$ , and  $k_z$  are non-negative integers),  $f_i$  is the PDF along  $\mathbf{e}_i$  and  $f_i^{eq}$  is the corresponding equilibrium PDF,  $\delta_t$  is the time step (the grid size  $\delta_x = c\delta_t$ ), and the dimensionless relaxation parameter  $\tau_f$  is related to the kinematic viscosity as  $\tau_f = 0.5 + \nu/(c_s^2 \delta_t)$  with  $c_s$  being the sound speed in LBM (usually  $c_s = c/\sqrt{3}$ ). The macroscopic variables, including the density  $\rho$  and the momentum  $\rho \mathbf{u}$ , are found from the PDFs as  $\rho = \sum_i f_i$  and  $\rho \mathbf{u} = \sum_i f_i \mathbf{e}_i$ . The pressure is tied to the density as  $p = \rho c_s^2$ . By applying the Chapman-Enskog expansion analysis, one can find that the LBEs recover the following macroscopic equations (up to the second order in the Knudsen number) [8]:

$$\partial_t \rho = -\partial_\alpha (\rho u_\alpha), \quad (2)$$

$$\partial_t (\rho u_\alpha) = -\partial_\beta (\rho u_\alpha u_\beta + p \delta_{\alpha\beta}) + \nu \partial_\beta \partial_\beta (\rho u_\alpha) + \frac{\nu}{c_s^2} \partial_\beta \partial_t (\rho u_\alpha u_\beta + p \delta_{\alpha\beta}) + 2\nu \partial_\alpha [\partial_\gamma (\rho u_\gamma)]. \quad (3)$$

If Taylor series expansion analysis is applied to the LBEs, the equations to update the density and momentum read [8]

$$\rho(\mathbf{x}, t + \delta_t) = \rho(\mathbf{x}, t) - \delta_t \partial_\alpha (\rho u_\alpha) + \frac{1}{2} \delta_t^2 \partial_\alpha \partial_\beta (\rho u_\alpha u_\beta + p \delta_{\alpha\beta}) + O(\delta_t^3), \quad (4)$$

$$\begin{aligned} \rho u_\alpha(\mathbf{x}, t + \delta_t) = & \rho u_\alpha(\mathbf{x}, t) - \delta_t \partial_\beta (\rho u_\alpha u_\beta + p \delta_{\alpha\beta}) + v \delta_t \partial_\beta \partial_\beta (\rho u_\alpha) \\ & + \left( \frac{v}{c_s^2} - 0.5 \delta_t \right) \delta_t \partial_t \partial_\beta (\rho u_\alpha u_\beta + p \delta_{\alpha\beta}) + 2v \delta_t \partial_\alpha [\partial_\gamma (\rho u_\gamma)] + O(\delta_t^3). \end{aligned} \quad (5)$$

These equations were claimed to be more actual and reasonable [8]. When compared with the weakly compressible NSEs, the underlined terms are SATs that help stabilize the simulation. Note that Eqs. (4) and (5) are partially discrete in time and a predictor-corrector procedure was applied to handle the time derivative on the right-hand side (r.h.s.) of Eq. (5). Specifically, the predictor step includes

$$\rho^* = \rho^n - \delta_t \partial_\alpha (\rho u_\alpha)^n + 0.5 \delta_t^2 \partial_\alpha \partial_\beta (\rho u_\alpha u_\beta + p \delta_{\alpha\beta})^n, \quad (6)$$

$$(\rho u_\alpha)^* = (\rho u_\alpha)^n - \delta_t \partial_\beta (\rho u_\alpha u_\beta + p \delta_{\alpha\beta})^n + v \delta_t \partial_\beta \partial_\beta (\rho u_\alpha)^n + 2v \delta_t \partial_\alpha [\partial_\gamma (\rho u_\gamma)^n], \quad (7)$$

and the corrector step includes

$$\rho^{n+1} = \rho^*, \quad (8)$$

$$(\rho u_\alpha)^{n+1} = (\rho u_\alpha)^* + \left( \frac{v}{c_s^2} - 0.5 \delta_t \right) [\partial_\beta (\rho u_\alpha u_\beta + p \delta_{\alpha\beta})^* - \partial_\beta (\rho u_\alpha u_\beta + p \delta_{\alpha\beta})^n]. \quad (9)$$

Since  $\rho^{n+1} = \rho^*$  and  $p = \rho c_s^2$ , the density and pressure are not modified in the corrector step and only the velocity changes. This predictor-corrector approach needs to compute and store the intermediate velocity  $u_\alpha^*$  and also has to calculate some derivatives of the intermediate variables [e.g.,  $\partial_\beta (\rho u_\alpha u_\beta)^*$ ]. It is noted that Eqs. (2) and (3) were unstable, whereas Eqs. (4) and (5) were stable when they are solved numerically by the same predictor-corrector procedure [8].

## B. Simplified MAMEs and its extension to thermal and two-phase flows

In general, when one solves the weakly compressible NSEs, the additional terms are *error terms that should be sufficiently small* so that they do not affect the accuracy of the numerical solutions. Unlike the original terms in the NSEs (which have certain physical meanings and must be strictly followed in the numerical solution), the SATs have *no real physical meanings* and their specific forms could possibly be adjusted. Of course, the adjustments must satisfy two requirements:

(1) The magnitude of the additional terms is small enough (thus not altering the true solution) and converges towards zero as  $\delta_x \rightarrow 0$  and  $\delta_t \rightarrow 0$

(2) Their stabilizing effect must be kept in the simulations with finite  $\delta_x$  and  $\delta_t$ .

In LBM simulation of incompressible flows (assuming  $c_s^2 = c^2/3$ ), one has

$$\partial_\beta (\rho u_\alpha u_\beta + p \delta_{\alpha\beta}) = c^2 [\partial_\beta (\rho u_\alpha u_\beta / c^2) + \partial_\alpha \rho / 3],$$

where the two terms in the square brackets are both of  $O(\text{Ma}^2)$ . When  $\partial_\beta (\rho u_\alpha u_\beta + p \delta_{\alpha\beta})$  appears in the SATs, it serves only to stabilize the computation and has no other roles. Thus, provided that both terms are of the same order, one may keep only one of them without changing the order of magnitude of the SATs (as a whole). From these arguments, one may

neglect  $\partial_\beta (\rho u_\alpha u_\beta)$  in the additional terms while satisfying the first requirement above. It seems difficult to prove that the omittance of  $\partial_\beta (\rho u_\alpha u_\beta)$  also satisfies the second requirement. Nevertheless, a number of tests, including both steady and unsteady, two-dimensional (2D) and three-dimensional (3D) problems, showed that the stabilizing effect was indeed still there. After neglecting  $\partial_\beta (\rho u_\alpha u_\beta)$ , the correction in Eq. (9) becomes

$$(1/c_s^2)(v - 0.5c_s^2 \delta_t) \partial_\alpha (p^* - p^n) = (v - 0.5c_s^2 \delta_t) (\partial_\alpha \rho^* - \partial_\alpha \rho^n).$$

Besides, the additional term  $2v \delta_t \partial_\alpha (\partial_\gamma (\rho u_\gamma))$  in Eq. (7) can be approximated as

$$2v \delta_t \partial_\alpha (-\partial_t \rho) = -2v \partial_\alpha (\delta_t \partial_t \rho) \approx -2v (\partial_\alpha \rho^{n+1} - \partial_\alpha \rho^n),$$

by using the continuity equation. Using all these approximations and combining the predictor and corrector steps, we propose the following semidiscrete equations for the weakly compressible NSEs with  $p = \rho c_s^2$ :

$$\rho^{n+1} = \rho^n - \delta_t \partial_\alpha (\rho u_\alpha)^n + \underline{0.5c_s^2 \delta_t^2 \partial_\alpha \rho^n}, \quad (10)$$

$$\begin{aligned} (\rho u_\alpha)^{n+1} = & (\rho u_\alpha)^n - \delta_t \partial_\beta (\rho u_\alpha u_\beta + \rho c_s^2 \delta_{\alpha\beta})^n + v \delta_t \partial_\beta \partial_\beta (\rho u_\alpha)^n \\ & \times \underline{-(v + 0.5c_s^2 \delta_t) (\partial_\alpha \rho^{n+1} - \partial_\alpha \rho^n)}. \end{aligned} \quad (11)$$

The remaining spatial derivatives are discretized by the second-order centered schemes, for example, in two dimensions:

$$\partial_x \rho|_{i,j} = (\rho_{i+1,j} - \rho_{i-1,j}) / (2\delta_x), \quad (12)$$

$$\begin{aligned} (\partial_x \partial_x \rho + \partial_y \partial_y \rho)|_{i,j} = & (\rho_{i+1,j} + \rho_{i-1,j} + \rho_{i,j+1} \\ & + \rho_{i,j-1} - 4\rho_{i,j}) / \delta_x^2. \end{aligned} \quad (13)$$

The underlined terms in Eqs. (10) and (11) are the simplified SATs to stabilize the simulation, which involve only the derivatives of the density. Since  $\rho^{n+1}$  in Eq. (11) is directly

TABLE I. Comparisons between the LBEs, original MAMEs, and simplified MAMEs for incompressible flow simulations (assuming  $p = \rho c_s^2$ ). In the original MAMEs, the corrector step does not alter the density obtained in the predictor step (i.e.,  $\rho^{n+1} = \rho^*$ ), and they are regarded as one variable. For the LBEs, D2Q9 and D3Q19 velocity models are assumed for 2D and 3D cases, respectively. When counting the stabilizing terms, the Laplacian is treated separately (e.g., in two dimensions  $\partial_{\alpha\alpha}\rho = \partial_{xx}\rho + \partial_{yy}\rho$  has two terms). In the LBEs, no explicit stabilizing terms are added.

Method	LBEs	MAMEs	SMAMEs
Variables (2D)	$\rho, u, v, f_i$ ( $i = 0, 1, \dots, 8$ )	$\rho, u, v, u^*, v^*$	$\rho, u, v$
No. of variables (2D)	12	5	3
No. of evolution eqs. (2D)	9 (D2Q9)	5	3
No. of small stabilizing terms (2D)	N.A.	$5 + (2 + 6) \times 2 = 21$	$2 + 2 \times 2 = 6$
Variables (3D)	$\rho, u, v, w, f_i$ ( $i = 0, 1, \dots, 18$ )	$\rho, u, v, w, u^*, v^*, w^*$	$\rho, u, v, w$
No. of variables (3D)	23	7	4
No. of evolution eqs. (3D)	19 (D3Q19)	7	4
No. of small stabilizing terms (3D)	N.A.	$9 + (3 + 8) \times 3 = 42$	$3 + 2 \times 3 = 9$

found from Eq. (10), it is fully explicit and does not need intermediate variables. It is noted that the SATs in Eq. (10) resemble that in the pressure evolution equation in Ref. [4] (the coefficient before  $\partial_{\alpha}\partial_{\alpha}\rho^n$  differs). It was mentioned in Ref. [4] that such an additional term was added to overcome the checkerboard instability for the pressure. We note that Eq. (10) also resembles the pressure equation in the EDAC [14] and the GPE in Refs. [12,19], both of which contain a dissipation term proportional to the Laplacian of the pressure. The SATs in Eq. (11) stabilize the simulation most likely in a way similar to the dissipation due to the bulk viscosity [13,20] though it looks to be somewhat different. We argue that this particular form may be better as it involves only the density (pressure) gradient, which is already calculated for Eq. (11) (in contrast, the other forms require the gradient of velocity divergence). When there is a body force  $g_{\alpha}$  along the  $x_{\alpha}$  direction, one only has to add a term  $\delta_t \rho^{n+1} g_{\alpha}$  on the r.h.s. of Eq. (11). Like the LBM, our method also uses the collocated arrangement of discrete variables in space. Table I compares the LBEs, the MAMEs [8], and the present SMAMEs (for simplified MAMEs).

In addition to the above simplifications, we also extend the proposed method to thermal flows with small temperature variations that allow the use of Boussinesq approximation as well as to two-phase flows with uniform density and viscosity. For the thermal flows (only 2D problems are considered), a forcing term  $\rho_0 g \beta (T - T_0)$  is added to the momentum equation in the  $y$  direction to account for the buoyancy effect where  $\rho_0$  is the reference density,  $g$  is the gravitational acceleration,  $T_0$  is the average temperature, and  $\beta$  is the thermal expansion coefficient [21]. Another evolution equation for the temperature is solved to provide  $T$  to calculate the forcing term [22,23],

$$\partial_t T + u_{\alpha} \partial_{\alpha} T = (\nu/\text{Pr}) \partial_{\alpha} \partial_{\alpha} T, \quad (14)$$

where Pr is the Prandtl number. On a solid wall with a unit normal vector  $\mathbf{n}_w$  the no flux condition  $\partial_{\mathbf{n}_w} T = 0$  is applied if the wall is adiabatic and the Dirichlet condition  $T = T_w$  is applied if the wall temperature is fixed at  $T_w$ . For two-phase flows, both fluids have the same density  $\rho_0$  and kinematic viscosity  $\nu$ . A phase field model is employed to deal with the interfaces and surface tension forces [24,25]. The two immiscible fluids are distinguished by an order parameter  $\phi$ .

In one fluid,  $\phi = 1$ , and in the other,  $\phi = -1$ . A thin transition region of width  $W$  exists between the two fluids. The contour lines (or isosurfaces) for  $\phi = 0$  are taken as the interfaces. Another term  $\delta_t F_{ST,\alpha} = -\delta_t \phi \partial_{\alpha} \mu$  is added on the r.h.s. of Eq. (11) to account for the surface tension effect. Here

$$\mu = 4a\phi(\phi^2 - 1) - \kappa \partial_{\alpha} \partial_{\alpha} \phi \quad (15)$$

is the chemical potential and the evolution of  $\phi$  is governed by the Cahn-Hilliard equation (CHE) [24,26],

$$\partial_t \phi + u_{\alpha} \partial_{\alpha} \phi = M \partial_{\alpha} \partial_{\alpha} \mu. \quad (16)$$

Here  $M$  is the mobility, and  $a$  and  $\kappa$  are two constants related to the surface tension  $\sigma$  and interface width  $W$  as

$$a = 3\sigma/(4W), \quad \kappa = 3\sigma W/8. \quad (17)$$

On a solid wall with a contact angle  $\theta$ , the no flux condition  $\partial_{\mathbf{n}_w} \mu = 0$  is applied for the chemical potential and the wetting boundary condition

$$\partial_{\mathbf{n}_w} \phi = -(2/W) \cos \theta (1 - \phi_w^2) \quad (18)$$

is applied for the order parameter ( $\phi_w$  is the order parameter at the wall) [27]. The spatial derivatives in Eqs. (14) and (16) are discretized by the second-order isotropic schemes and the time marching uses the second-order RK scheme. Specifically, the isotropic schemes to compute the spatial derivatives are given by [28]

$$\partial_{\alpha} \phi = \frac{3}{c \delta_x} \sum_{i=1}^b w_i e_{i\alpha} \phi(\mathbf{x} + \mathbf{e}_i \delta_t), \quad (19)$$

$$\nabla^2 \phi = \frac{6}{\delta_x^2} \left[ \sum_{i=1}^b w_i \phi(\mathbf{x} + \mathbf{e}_i \delta_t) - (1 - w_0) \phi(\mathbf{x}) \right], \quad (20)$$

where the lattice velocity (magnitude)  $c$  is  $c = \delta_x / \delta_t = \sqrt{3} c_s$ ,  $\mathbf{e}_i$  ( $i = 0, 1, \dots, b$ ) is the lattice velocity (vector) (e.g.,  $b = 8$  for the D2Q9 velocity model and  $b = 18$  for D3Q19), and  $w_i$  is the weight for different lattice velocities. It should be noted that for two-phase flows the real fluid density  $\rho_0$  is a constant (set to 1), whereas  $\rho = p/c_s^2$  has small variations around its initial value (also set to 1).

TABLE II. Comparisons between the MAMEs, SMAMEs, KRLNS, EDAC, and GPE. Abbreviations used: eqs., equations; artif. dissip., artificial dissipation; FD, finite difference; pred.-corr., predictor-corrector; FE, forward Euler. Note that (1) in the KRLNS “pressure diffusion” is replaced by the grand potential diffusion; (2) the MacCormack scheme ties the spatial and temporal discretizations together, and the time stepping is similar to a predictor-corrector procedure.

Method	MAMEs	SMAMEs	KRLNS	EDAC	GPE
Governing eqs.	Discrete in time			Continuous in space and time	
Pressure diffusion	Numerical			Physical	
Form of diffusion	$\partial_\beta \partial_\beta p + \partial_\alpha \partial_\beta (\rho u_\alpha u_\beta)$	$\partial_\beta \partial_\beta p$	$\partial_\beta \partial_\beta \mathcal{G}$		$\partial_\beta \partial_\beta p$
Diffusion coefficient	$0.5c_s^2 \delta_t$ (Re-independent)			$\nu$ (1/Re)	
Origin of diffusion term	LBEs			Energy eq. of compressible NSEs	
Bulk viscosity terms	Kept in momentum eqs.			Neglected in momentum eqs.	
Form of artif. dissip.	Explicit			Hidden in numerical schemes	
Origin of artif. dissip.	LBEs			Discretization schemes	
Spatial discretization	centered FD		MacCormack [11,14]		Centered FD (staggered)
Time stepping	pred.-corr.	FE-like	MacCormack [11,14]		RK

### C. Comparison with the KRLNS, EDAC and GPE

As noted in Sec. I, there exist some other methods in the ACM framework such as the KRLNS, EDAC, and GPE. Although belonging to the general ACM category, the MAMEs and SMAMEs differ from them in a few aspects (see Table II for an overview).

First, the MAMEs are a set of *semidiscrete* equations [Eqs. (4) and (5)] derived from the LBEs that specify the rule to update the local density and momentum [i.e.,  $\rho(t) \rightarrow \rho(t + \delta_t)$ ,  $\rho u_\alpha(t) \rightarrow \rho u_\alpha(t + \delta_t)$ ]. To carry out a simulation, one has to perform *only spatial discretizations* in principle (though a predictor-corrector procedure was used to handle the time derivatives in the SATs in the original MAMEs). The present SMAMEs inherits this feature [see Eqs. (10) and (11)] and avoids the predictor-corrector procedure. The KRLNS, EDAC and GPE are all continuum methods using *continuous* governing equations. To use them, one has to perform *both spatial and temporal discretizations*.

Second, the diffusion in the pressure equation is different. To facilitate the comparison, we first multiply Eqs. (6) [together with Eq. (8)] and (10) with  $c_s^2$  ( $\rho c_s^2 = p$ ) and obtain the pressure evolution equations for the MAMEs and SMAMEs as

$$p^{n+1} = p^n - \delta_t \partial_\alpha (p u_\alpha)^n + 0.5c_s^2 \delta_t^2 \partial_\alpha \partial_\beta (\rho u_\alpha u_\beta + p \delta_{\alpha\beta})^n, \quad (21)$$

$$p^{n+1} = p^n - \delta_t \partial_\alpha (p u_\alpha)^n + 0.5c_s^2 \delta_t^2 \partial_{\alpha\alpha} p^n. \quad (22)$$

The last term on the r.h.s. of Eq. (21) is the diffusion term obtained from the Taylor series expansion of the LBEs [8], and that in Eq. (22) is simplified from Eq. (21) by dropping the velocity-related terms. In the KRLNS, EDAC, and GPE, the evolution equations for the pressure or grand potential are derived from the energy equation under low Mach numbers [9,14,19]. With some assumptions, the simplified governing equations in dimensionless form in the KRLNS are [11]

$$\partial_t \mathcal{G} = -\frac{1}{M_a^2} \partial_\alpha u_\alpha + \frac{1}{\text{Re}} \partial_\beta \partial_\beta \mathcal{G}, \quad (23a)$$

$$\partial_t u_\alpha = -\partial_\beta (u_\alpha u_\beta) - \partial_\alpha p + \frac{1}{\text{Re}} \partial_\beta \partial_\beta u_\alpha, \quad (23b)$$

where  $\mathcal{G} = p - u_\alpha u_\alpha / 2$  is the grand potential (the density is taken as 1) and Re is the Reynolds number. The EDAC differs from the KRLNS with Eq. (23a) for the grand potential  $\mathcal{G}$  replaced by another evolution equation for the pressure  $p$  [14]:

$$\partial_t p + u_\alpha \partial_\alpha p = -\frac{1}{M_a^2} \partial_\alpha u_\alpha + \frac{1}{\text{Re}} \partial_\beta \partial_\beta p. \quad (24)$$

The GPE differs from the KRLNS by using another pressure evolution equation (assuming that the Prandtl number and specific heat ratio are both 1) [12],

$$\partial_t p = -\frac{1}{M_a^2} \partial_\alpha u_\alpha + \frac{1}{\text{Re}} \partial_\beta \partial_\beta p, \quad (25)$$

which lacks the convection term  $u_\alpha \partial_\alpha p$  on the left-hand side as compared with the EDAC. Although all five methods have some diffusion included in the evolution equation for the pressure (or grand potential), the form of the diffusion term and the diffusion coefficient in the MAMEs differ from those in the KRLNS, EDAC, and GPE. The SMAMEs lies somewhere in between the MAMEs and the other three methods: it has a simple form of diffusion (like the KRLNS, EDAC, and GPE) and uses the same diffusion coefficient as the MAMEs. In the MAMEs and SMAMEs, the diffusion coefficient is  $0.5c_s^2 \delta_t = (1/6)(\delta_x^2 / \delta_t)$  [assuming  $c_s = c / \sqrt{3} = \delta_x / (\sqrt{3} \delta_t)$ ], whereas in the KRLNS, EDAC, and GPE the diffusion coefficient is  $1/\text{Re}$  (in dimensional form it is the kinematic viscosity  $\nu$ ). In ACM simulations of incompressible flows, the time step usually should satisfy  $\delta_t \sim O(\delta_x^2)$ . Therefore, the diffusion coefficient in the MAMEs and SMAMEs is  $(1/6)(\delta_x^2 / \delta_t) \sim O(1)$  and independent of the Reynolds number. The differences in the diffusion term are ultimately connected with the different origins. As noted before, in the continuum methods the pressure evolution equation is derived from the (*continuum*) energy equation [9,14,19], whereas in the MAMEs it is found through Taylor series analysis of the (*discrete*) LBEs [8]. Thus, in the continuum methods the diffusion has more *physical* meanings, but in the MAMEs and SMAMEs it has no physical meanings and is purely *numerical*.

Third, in the KRLNS, EDAC, and GPE, the bulk viscosity terms are neglected in the momentum equations [10–12,14]. Unlike them, the MAMEs keeps such terms (appearing as

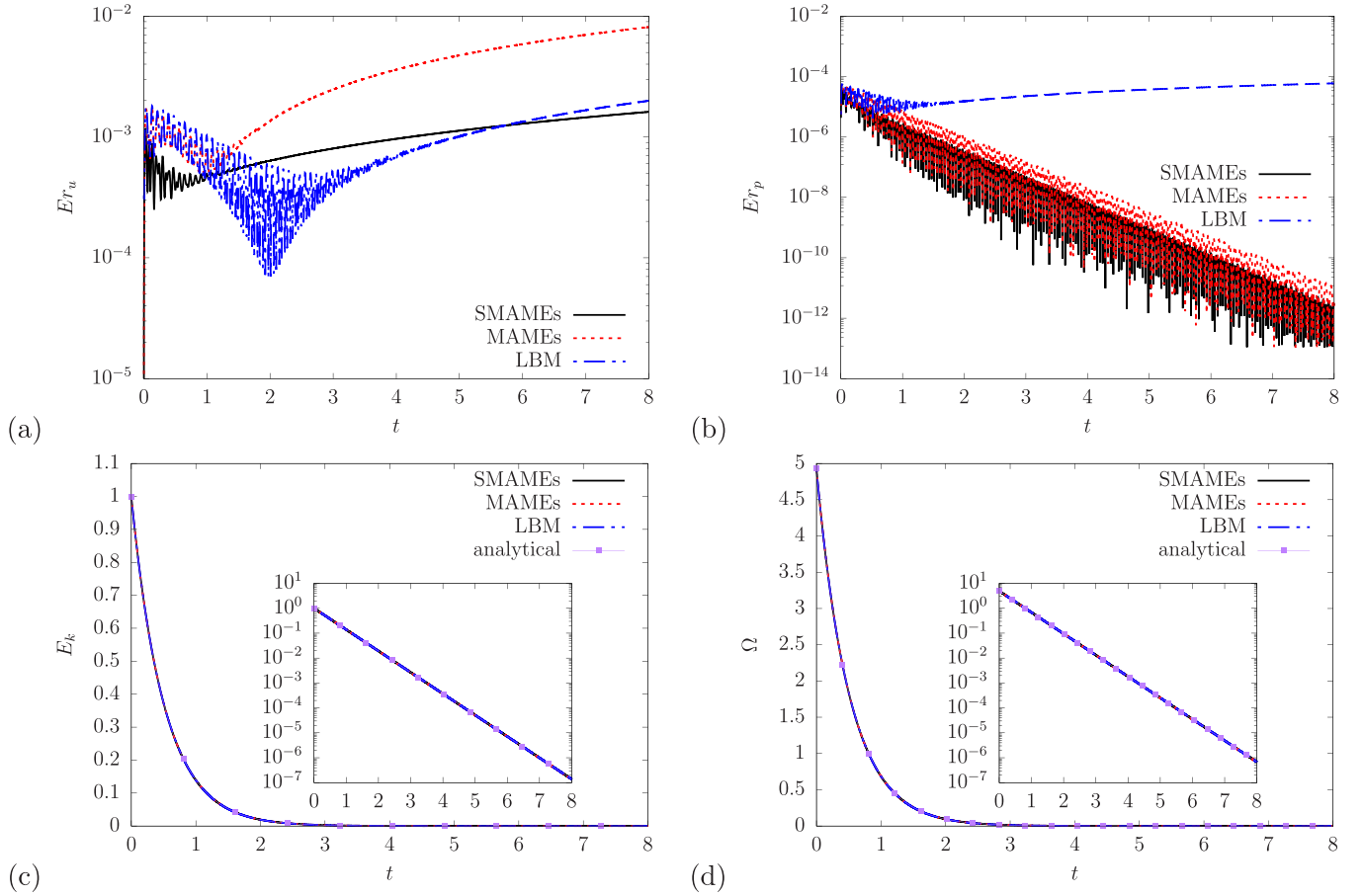


FIG. 1. Evolutions of (a) the error in the horizontal velocity component  $Er_u$ , (b) the error in the pressure  $Er_p$ , (c) the total kinetic energy  $E_k$ , and (d) the total entropy  $\Omega$  in the simulation of the 2D Taylor-Green vortex. The Reynolds number is  $Re = 20$  and the shared simulation parameters are  $N_L = 50$  and  $N_t = 1000$  ( $c = 20$ ). The solid line is by the present method, the dashed line is by the original MAMEs and the dash-dot-dot line is by the LBM using MRT. In (c), (d) the insets give the plots of the same data with the axis for  $E_k$  and  $\Omega$  in log scale, and the analytical predictions are given by the line with filled squares.

SATs) with the specific forms derived from the LBEs and the SMAMEs also retains similar terms but with certain simplifications. As will be shown in Sec. III A, the SATs in the momentum equations are crucial to stabilize the simulation if the spatial derivatives are discretized by simple centered schemes and the variables are updated in time in the simplest explicit way. Without any SATs in the momentum equations, the success of KRLNS, EDAC and GPE relies on other numerical components. For instance, the MacCormack scheme is commonly used in the KRLNS and EDAC [11,14], and this scheme itself has certain numerical dissipation to stabilize the computation. There may be some other choices of the schemes, for example, the KRLNS in Ref. [10] used the spectral element method with mixed explicit-implicit operator splitting for time integration to stabilize the computation. The GPE uses staggered grid together with a RK time stepping to avoid the unstable problem [12]. In other words, the MAMEs and SMAMEs have the artificial dissipation terms *explicitly expressed* in the semidiscrete momentum equations and then discretize them by simple centered schemes, whereas in the other three continuum methods the artificial dissipation is *hidden* in more complicated numerical schemes to discretize the continuum equations in both space and time. It is noted that in

some numerical methods to solve the compressible NSEs the artificial dissipation terms may also be explicitly given (e.g., the Jameson-Schmidt-Turkel scheme [29]), and they can be used in the ACM for incompressible flow simulations as well (e.g., see [30]).

### III. RESULTS AND DISCUSSION

In this section, we present the results of several test cases obtained by using our method and make comparisons with those in the literature and by other methods under the same simulation settings (i.e., same  $\delta_x$  and  $\delta_t$ ). Note that the LBM simulations below use the D2Q9 and D3Q19 velocity models for 2D and 3D problems, respectively, and the multiple relaxation time (MRT) [31] or the weighted MRT model [32] for the collision step. Uniform mesh and time step are used in all problems. For each problem, a characteristic length  $L$  and characteristic velocity  $U_c$  are chosen. The characteristic time  $T_c = L/U_c$  is divided into  $N_t$  segments ( $\delta_t = T_c/N_t$ ) and the characteristic length  $L$  is discretized into  $N_L$  segments ( $\delta_x = L/N_L$ ).

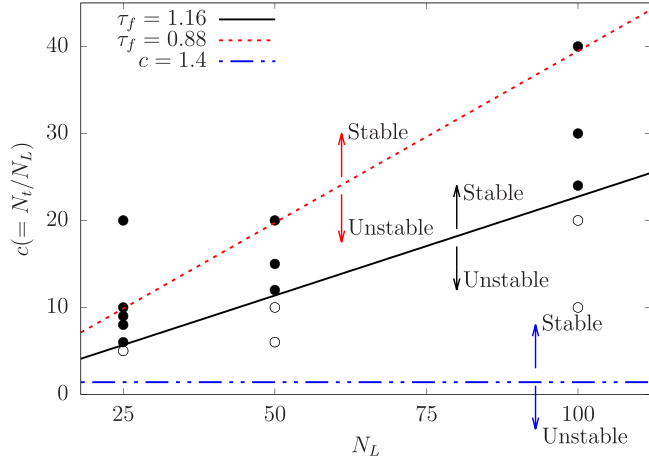


FIG. 2. Stable and unstable regions in the  $N_L$ - $c$  plane for different methods to simulate the Taylor-Green vortex problem at  $\text{Re} = 20$ . Note the grid size  $\delta_x = 1/N_L$  and the time step  $\delta_t = 1/N_t = 1/(cN_L)$ . The three lines approximately represent the critical conditions for the present method (solid), the original MAMEs (dashed) and the LBM using MRT (dash-dot-dot). The stable regions are above the respective lines, and the unstable regions are below them. The filled circles represent the stable cases, and the empty circles represent the unstable cases for the present method (for clarity, the specific data for the other two methods are not plotted). The tests were performed for  $0 \leq t \leq 4$ . In the stable runs the errors do not increase abruptly. For the LBM runs, the MRT parameters follow those in Fig. 1 of [31], and the errors are quite large when  $c$  is too small (even though the runs do not blow up).

### A. Taylor-Green vortex in two and three dimensions

The first case is the Taylor-Green vortex (TGV) in two and three dimensions. First, we consider the 2D TGV. The analytical solutions for this problem in the domain  $[-1, 1] \times [-1, 1]$

(i.e., the characteristic length  $L = 1$ ) with a characteristic velocity  $u_0$  (set to 1) are given by [8]

$$u_{\text{analytical}}(x, y, t) = -u_0 \cos(\pi x/L) \sin(\pi y/L) \times \exp(-2\pi^2 t/\text{Re}), \quad (26a)$$

$$v_{\text{analytical}}(x, y, t) = u_0 \sin(\pi x/L) \cos(\pi y/L) \exp(-2\pi^2 t/\text{Re}), \quad (26b)$$

$$p_{\text{analytical}}(x, y, t) = p_0 - 0.25\rho_0 u_0^2 [\cos(2\pi x/L) + \cos(2\pi y/L)] \times \exp[-4\pi^2 u_0 t/(\text{Re}L)]. \quad (26c)$$

where  $\text{Re} = u_0 L/\nu$  is the Reynolds number,  $\rho_0$  is the density (set to 1), and  $p_0$  is the reference pressure (set to  $p_0 = \rho_0 c_s^2$ ). From Eqs. (26a) and (26b), the analytical solution for the vorticity  $\omega = \partial_x v - \partial_y u$  can be derived,

$$\omega_{\text{analytical}}(x, y, t) = 2(\pi/L)u_0 \cos(\pi x/L) \cos(\pi y/L) \times \exp(-2\pi^2 t/\text{Re}). \quad (27)$$

This problem is periodic in both the  $x$  and  $y$  directions. The initial fields are set according to Eqs. (26a)–(26c) with  $t = 0$ . The case at  $\text{Re} = 20$  (same as [8]) is studied.

We mainly focus on the error in the numerical solutions of the velocity component  $u$  and the pressure  $p$  defined as follows:

$$\text{Er}_u(t) = \frac{\sqrt{\sum_{i,j} [u_{\text{numerical}}(x_{i,j}, y_{i,j}, t) - u_{\text{analytical}}(x_{i,j}, y_{i,j}, t)]^2}}{\sqrt{\sum_{i,j} u_{\text{analytical}}^2(x_{i,j}, y_{i,j}, t)}}, \quad (28)$$

$$\text{Er}_p(t) = \frac{\sqrt{\sum_{i,j} [p_{\text{numerical}}(x_{i,j}, y_{i,j}, t) - p_{\text{analytical}}(x_{i,j}, y_{i,j}, t)]^2}}{\sqrt{\sum_{i,j} p_{\text{analytical}}^2(x_{i,j}, y_{i,j}, t)}}, \quad (29)$$

where the summation is for all nodes in the simulation domain. Note the error  $\text{Er}_v(t)$  is the same as  $\text{Er}_u(t)$  due to the

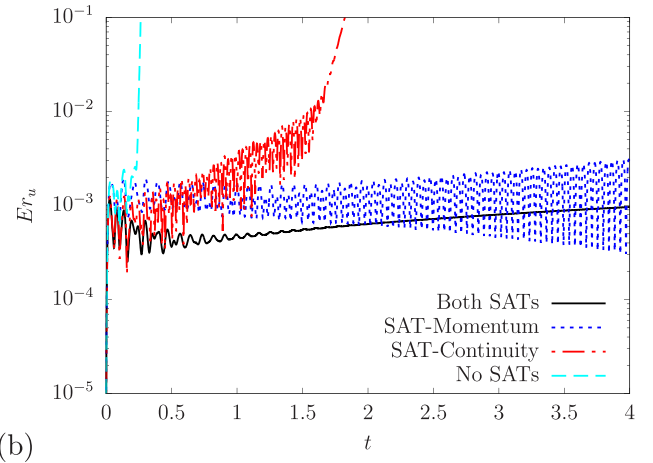
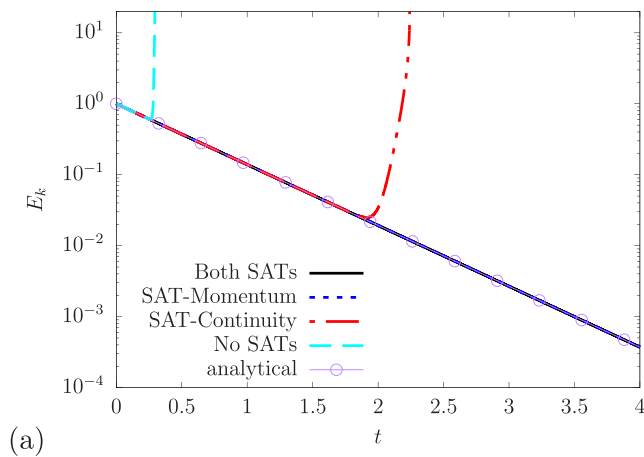


FIG. 3. Evolutions of (a) the total kinetic energy  $E_k$  (b) the error in the horizontal velocity component  $\text{Er}_u$ . The solid line was obtained with both the SATs in Eqs. (10) and (11), the dashed line was obtained with the SATs in the momentum equations [Eq. (11)] only, the dash-dot-dot line was obtained with the SAT in the continuity equation [Eq. (11)] only, and the long-dashed line was obtained without any SAT. The shared simulation parameters are  $N_L = 50$  and  $N_t = 1000$  ( $c = 20$ ).

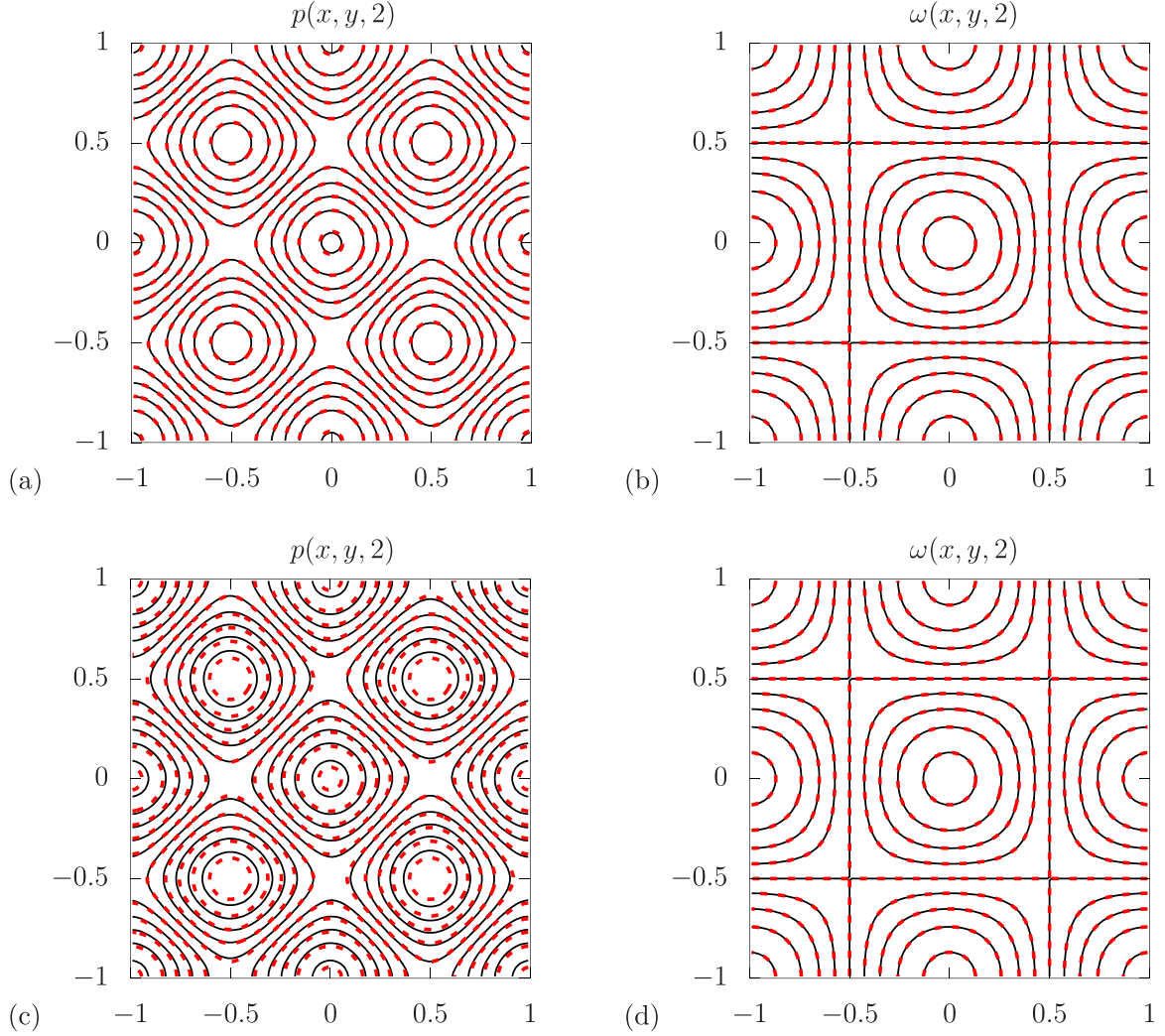


FIG. 4. Contour plots of (a), (c) the pressure field and (b), (d) the vorticity field at  $t = 2.0$  in the simulation of the 2D Taylor-Green vortex at  $Re = 20$ . The simulation parameters are  $N_L = 50$  and  $N_t = 1000$  ( $c = 20$ ). The black solid line is by the present method, and the red dashed line is the analytical solution. The results in (a), (b) were obtained with the SATs added in both the continuity and momentum equations, whereas those in (c), (d) were obtained with the SATs in the momentum equations only.

symmetry of this problem. Besides, the total kinetic energy  $E_k$  and enstrophy  $\Omega$  were also monitored during the simulation, and they are calculated as

$$E_k = \frac{1}{2S} \int_S (u^2 + v^2) dS \approx \frac{1}{2S} \sum_{i,j} (u_{i,j}^2 + v_{i,j}^2) dS_{i,j},$$

$$\Omega = \frac{1}{2S} \int_S \omega^2 dS \approx \frac{1}{2S} \sum_{i,j} \omega_{i,j}^2 dS_{i,j}, \quad (30)$$

where  $S$  is the total area of the domain,  $dS_{i,j}$  is the area of the cell labeled by the indices  $(i, j)$ ,  $u_{i,j}$ ,  $v_{i,j}$ , and  $\omega_{i,j}$  are the  $x$ -velocity and  $y$ -velocity components and vorticity at the node  $(i, j)$ , respectively, and the summation is performed over all the nodes within the domain. From the analytical solution, one can find that  $E_k$  and  $\Omega$  depend on  $t$  as

$$E_k(t) = u_0^2 \exp(-4\pi^2 t/Re),$$

$$\Omega(t) = \frac{1}{2} \pi^2 \frac{u_0^2}{L^2} \exp(-4\pi^2 t/Re). \quad (31)$$

Figure 1 shows the evolutions of  $Er_u$ ,  $Er_p$ ,  $E_k$ , and  $\Omega$  over a relatively long period of time ( $0 \leq t \leq 8$ ) by using the present method (SMAMEs), the original MAMEs in Ref. [8] and the LBM (using MRT [31]). For the LBM, the model parameters for MRT follow those in Fig. 1 of [31]. It is seen that for all three methods the deviations in  $u$  remain small (around  $10^{-3}$ ) in the early stage ( $t < 1$ ), but after some time the deviations grow with time. At the end of simulation ( $t = 8$ ), the present method and LBM can still have reasonably good accuracy [ $O(10^{-3})$ ] whereas the original MAMEs give less satisfactory results [ $O(10^{-2})$ ]. For the pressure field, the deviations always remain to be small (less than  $10^{-4}$ ) for all three methods, and both the SMAMEs and MAMEs can make  $Er_p$  keep decreasing to as low as about  $10^{-12}$ . The predictions of the total kinetic energy  $E_k$  and enstrophy  $\Omega$  by the three methods are all very close to the analytical results, as seen from Figs. 1(c) and 1(d). With the same simulation parameters ( $N_L = 50$  and  $c = 20$ ), the computation times are 18.0 s, 23.3 s and 34.2 s for the present SMAMEs, the original MAMEs, and the

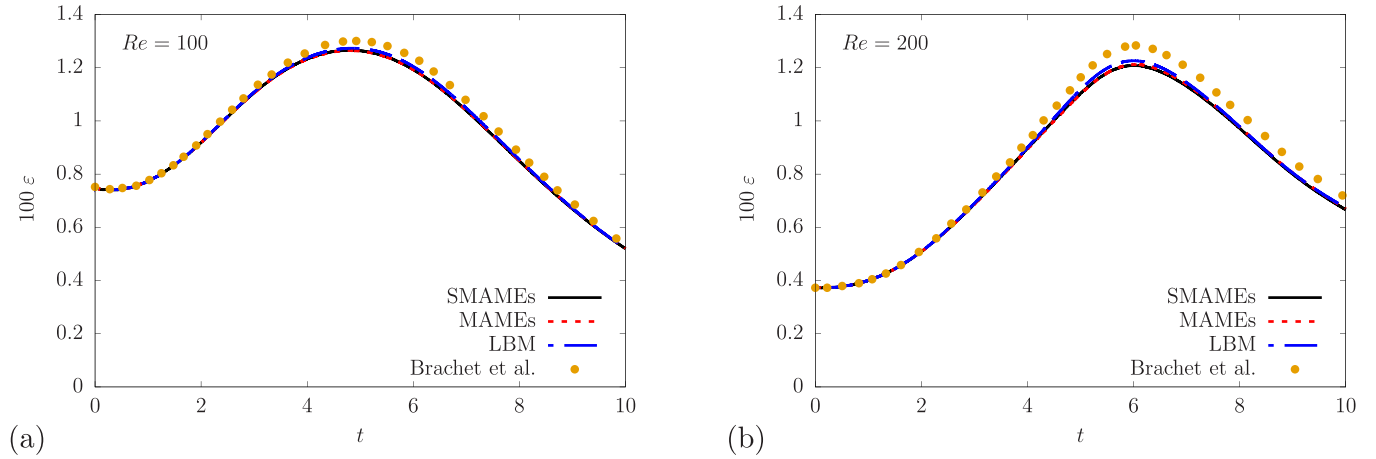


FIG. 5. Evolutions of the rate of energy dissipation  $\varepsilon(t)$  at (a)  $Re = 100$  and (b)  $Re = 200$  for the 3D Taylor-Green vortex. The solid line is by the present SMAMEs simulation, the dashed line is by the original MAMEs, and the dash-dot-dot line is by the 3D LBM (D3Q19) using the weighted MRT collision model [32]. The filled circles are by the spectral methods from [36]. The shared simulation parameters for the SMAMEs, MAMEs, and LBM are  $N_L \approx 20.372$  ( $128^3$  grid points) and  $N_t \approx 407.437$  ( $c = 20$ ).

MRT-LBM, respectively. That is, the present method saves about 25% of the time compared to the original MAMEs, and it saves nearly one half of the time compared to the MRT-LBM. At the same time, it is as accurate as the MRT-LBM and more accurate than the original MAMEs. It is noted that the velocity magnitude at  $t = 8$  has decreased by three orders of magnitude (compared to its initial value), and it may be more difficult to closely follow the analytical solutions.

Figure 2 shows the stability diagram in the  $N_L$ - $c$  plane for three methods (SMAMEs, MAMEs, and LBM) for the same case at  $Re = 20$ . It is seen that the stable region of the present method is larger on this map than that of the original method using the MAMEs. In other words, under the same grid size, the present method can use a larger time step than the original method in Ref. [8]. The difference in the minimal  $c$  (or the maximal  $\delta_t$ ) for a stable computation between the two methods increases as  $N_L$  increases (i.e., the grid size  $\delta_x$  decreases). Among the three methods being compared, the LBM is the most stable and the minimal  $c$  (to keep the simulation stable) is almost constant when the mesh is refined. However, it does not mean that the LBM can give reliable results irrespective of the lattice velocity  $c$ . In fact, the LBM for incompressible flow simulations should follow the diffusive scaling [ $\delta_x \sim O(\epsilon)$  and  $\delta_t \sim O(\epsilon^2)$ ] [6,33,34]. That means the lattice velocity  $c$  should satisfy  $c \sim O(1/\epsilon) \sim O(N_L)$ . Thus, even though LBM remains stable when  $c \sim O(1)$ , it does not satisfy the requirement for the simulation of incompressible flows. Overall, in terms of the stability performance, the present method is in between the original MAMEs and the LBM according to Fig. 2.

Next, the effects of the SATs in Eqs. (10) and (11) are investigated. Figure 3 compares the evolutions of  $E_k$  and  $Er_u$  for a typical case at  $Re = 20$  as obtained by using four different simulation settings (1) both the SATs in the continuity and momentum equations are included (2) only the SATs in the momentum equations are included (3) only the SATs in the continuity equation is included (4) no SATs are included. When the SATs are absent from Eqs. (10) and (11), both the kinetic energy and the error in  $u$  quickly become very

large. When the SAT in the continuity equation is added, the situation improves slightly but the simulation still goes unstable ( $E_k$  increases sharply) after some time. This indicates that the SATs in the momentum equations are crucial to maintain the stability. With the SATs only added in the momentum equations, the computation remains stable and the total kinetic energy follows the analytical prediction, but the error in  $u$  shows significant fluctuations. The reason may be that the SAT in the continuity equation, which is dissipative in nature, helps to damp out the oscillations in the density (pressure) field. In contrast to the above three situations, when the SATs in the continuity and momentum equations are both added, the simulation is not only stable but also shows the least fluctuations in  $Er_u$ . In addition, the contour plots of the pressure  $p$  and vorticity  $\omega$  at  $t = 2.0$  for the two stable simulations under settings (1) and (2) are shown in Fig. 4, together with the analytical predictions by Eqs. (26c) and (27). It is seen that the numerical solutions by the SMAMEs agree well with the analytical solutions when the SATs are added in both the continuity and momentum equations. When the SATs are added only in the momentum equations (but not in the continuity equation), the vorticity field still seems to follow the analytical solution whereas the difference in the pressure field becomes noticeable. As noted earlier, the SATs in Eqs. (10) and (11) are much simplified compared with the original MAMEs in Ref. [8]. Yet they are sufficient to keep the computation stable and provide accurate results. This will be further demonstrated through other tests below. It seems that it is difficult to further simplify the SATs.

We also simulated the 3D TGV problem. The domain is a cubic box of side length  $L_B = 2\pi$ ,  $[0, 2\pi] \times [0, 2\pi] \times [0, 2\pi]$  [i.e., the characteristic length is  $L = L_B/(2\pi)$ ]. Periodic boundary conditions are applied in all three directions. The initial condition for the velocity  $\mathbf{u} = u\mathbf{e}_x + v\mathbf{e}_y + w\mathbf{e}_z$  is given by [35]

$$u(x, y, z, 0) = u_0 \cos(x) \sin(y) \cos(z), \quad (32a)$$

$$v(x, y, z, 0) = -u_0 \sin(x) \cos(y) \cos(z), \quad (32b)$$

$$w(x, y, z, 0) = 0, \quad (32c)$$

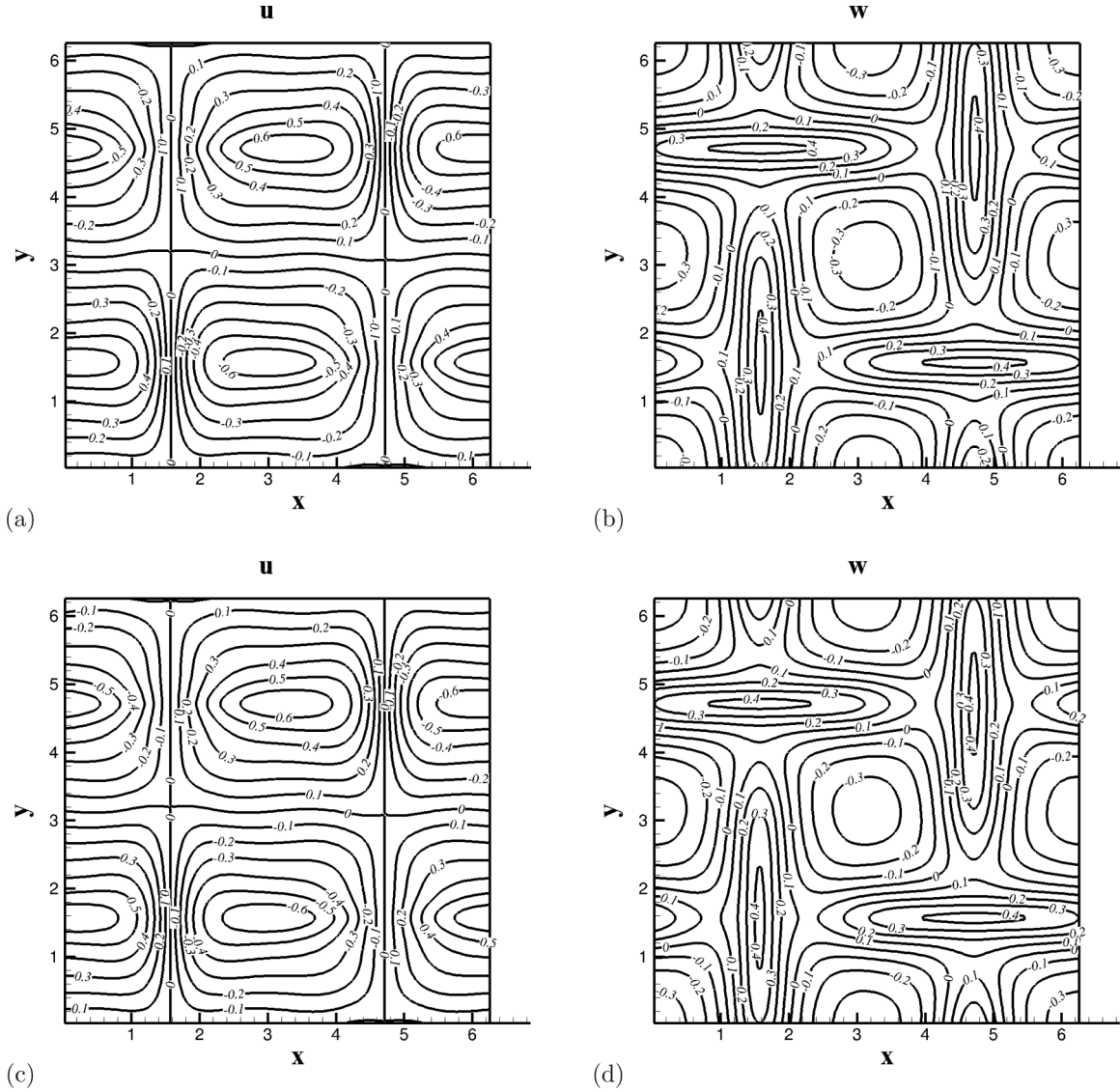


FIG. 6. Contour plots of the velocity components (a), (c)  $u$  and (b), (d)  $w$  at  $t = 3.5$  and  $Re = 100$  in the plane  $z = \pi/4$  for the 3D Taylor-Green vortex. The results by the SMAMEs are in the upper row whereas those by the original MAMEs are in the lower row. The shared simulation parameters for the SMAMEs and MAMEs are  $N_L \approx 20.372$  ( $128^3$  grid points) and  $N_r \approx 407.437$  ( $c = 20$ ).

where  $u_0 = 1$  (i.e., the characteristic velocity is chosen as  $u_0$ ). The initial pressure field is

$$p(x, y, z, 0) = p_0 + \frac{1}{16} \rho_0 u_0^2 [\cos(2z) + 2][\cos(2x) + \cos(2y)], \quad (33)$$

where  $\rho_0 = 1$  and  $p_0 = \rho_0 c_s^2$ . In the 3D TGV, we focus on the rate of energy dissipation  $\varepsilon(t)$  defined by

$$\varepsilon(t) = \frac{1}{Re} \overline{|\boldsymbol{\omega}|^2} = \frac{1}{Re} \frac{1}{(2\pi)^3} \int_0^{2\pi} \int_0^{2\pi} \int_0^{2\pi} \boldsymbol{\omega} \cdot \boldsymbol{\omega} dx dy dz. \quad (34)$$

where  $Re = u_0 L / \nu = 1/\nu$  is the Reynolds number,  $\boldsymbol{\omega} = \nabla \times \mathbf{u}$  is the vorticity and  $\overline{|\boldsymbol{\omega}|^2}$  is the mean-square vorticity [35]. Two cases at  $Re = 100$  and  $200$  were simulated with  $N_L \approx 20.372$  ( $128^3$  grid points) and  $c = 20$  by using the SMAMEs, MAMEs, and LBM. Note that LBM simulations use the D3Q19 velocity model and the weighted MRT collision model [32].

Figure 5 shows the evolutions of the rate of energy dissipation  $\varepsilon(t)$  for  $0 \leq t \leq 10$  at the two  $Re$  numbers. Previously, this problem was also simulated by the spectral method in Ref. [35] (with a resolution  $32^3$ ) and in Ref. [36] (with a resolution up to  $256^3$ ). The results from [36] are also plotted in Fig. 5 for comparison. It is seen that the present results by the SMAMEs are almost the same as those by the MAMEs, and are very close to the LBM results for both  $Re = 100$  and  $Re = 200$ . All three sets of results by current simulations at  $Re = 100$  are close to those in Ref. [36]. The differences between the present results and the reference ones in Ref. [36] are slightly larger at  $Re = 200$ , but still remain to be small. The possible reason may be that, as  $Re$  increases, more complex flow structures develop as time goes on and that requires better resolution. This deficiency (with respect to the spectral method) is inherent to all second-order methods, and a similar trend is observed for other methods with an order of accuracy

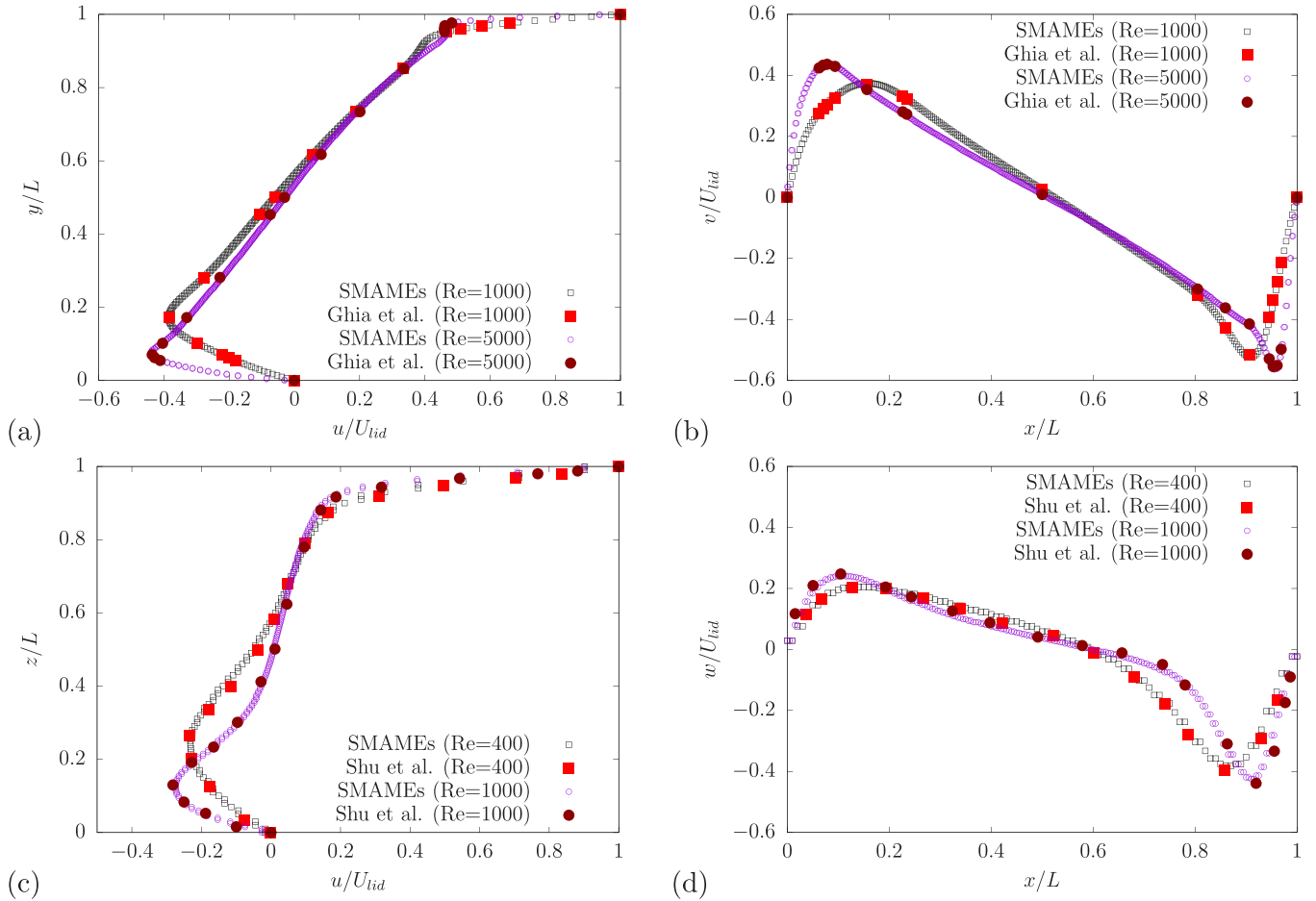


FIG. 7. Velocity profiles along the centerlines (a)  $u(y)$  at  $x = 0.5$  and (b)  $v(x)$  at  $y = 0.5$  for the 2D cases; (c)  $u(z)$  at  $x = 0.5$  and (d)  $w(x)$  at  $z = 0.5$  in the plane  $y = 0.5$  for the 3D cases. The reference data for the 2D cases are from [38], and those for the 3D cases are from [39].

higher than two (e.g., see Fig. 4 of [37]). In addition to  $\varepsilon(t)$ , the velocity components  $u$  and  $w$  in the plane at  $z = \pi/4$  at  $t = 3.5$  for the case at  $Re = 100$  were extracted, and their contour lines are shown in Fig. 6 (for the simulations by the SMAMEs and MAMEs). One can easily see from Fig. 6 that the two sets of results agree well with each other. It was also found that the present results resemble those by the spectral method from [35] (see Figs. 4 and 5 therein). Note that both  $u$  and  $w$  in Fig. 6 should be multiplied by 100 for comparison with [35]. Overall, the present SMAMEs results are as accurate as those by the MAMEs and LBM. For a typical 3D TGV case using the above simulation parameters ( $128^3$ ,  $c = 20$ ), the computation times cost by the SMAMEs, MAMEs and LBM (D3Q19, weighted MRT) are about 1093 s, 2641 s, and 2943 s (all using four nodes with the same domain decomposition on the same computer). It means that the present method is more than *two times faster* as compared to the MAMEs, and it is almost *three times faster* as compared to the LBM. As compared to the 2D cases, the saving of computation time by the SMAMEs is even more significant.

### B. Lid-driven cavity flow in two and three dimensions

The second case is the lid-driven cavity flow. Both 2D and 3D situations were studied. In two dimensions the

domain is a square  $[0, 1] \times [0, 1]$  enclosed by four solid walls (i.e., the side length  $L$  is chosen as the characteristic length). The top wall at  $y = 1$  is moving with a constant velocity  $(U_{lid}, 0) = (1, 0)$  (i.e., the lid velocity is chosen to be the characteristic velocity). In three dimensions the domain is a cube  $[0, 1] \times [0, 1] \times [0, 1]$ , and the top wall at  $z = 1$  is moving with a constant velocity  $(U_{lid}, 0, 0) = (1, 0, 0)$ . All other walls are stationary. The Reynolds number is given by  $Re = U_{lid}L/\nu$ . The initial fields are set to be  $u = v (= w) = 0$  and  $\rho = \rho_0 = 1$ . The criterion  $\max ||\mathbf{u}|^{n+1} - |\mathbf{u}|^n| < 10^{-8}$  is used to determine whether the steady state is reached (i.e., the change in the velocity magnitude between two consecutive steps is less than  $10^{-8}$  everywhere). Several cases commonly used for benchmark studies were investigated, including  $Re = 100, 400, 1000$ , and  $5000$  in two dimensions and  $Re = 100, 400$ , and  $1000$  in three dimensions. Here we present only the results of four cases at high  $Re$  numbers ( $Re = 1000$  and  $5000$  in two dimensions, and  $Re = 400$  and  $1000$  in three dimensions). For the 2D cases, the numerical parameters are  $N_L = 256$ ,  $c = 50$  for both  $Re = 1000$  and  $Re = 5000$ . For the 3D cases they are  $N_L = 64$ ,  $c = 20$  for  $Re = 400$  and  $N_L = 96$ ,  $c = 20$  for  $Re = 1000$ . Figure 7 gives the velocity profiles along selected centerlines for the four cases. The data from [38,39] are also plotted for comparison. The data from [38] were obtained by solving the incompressible NSEs

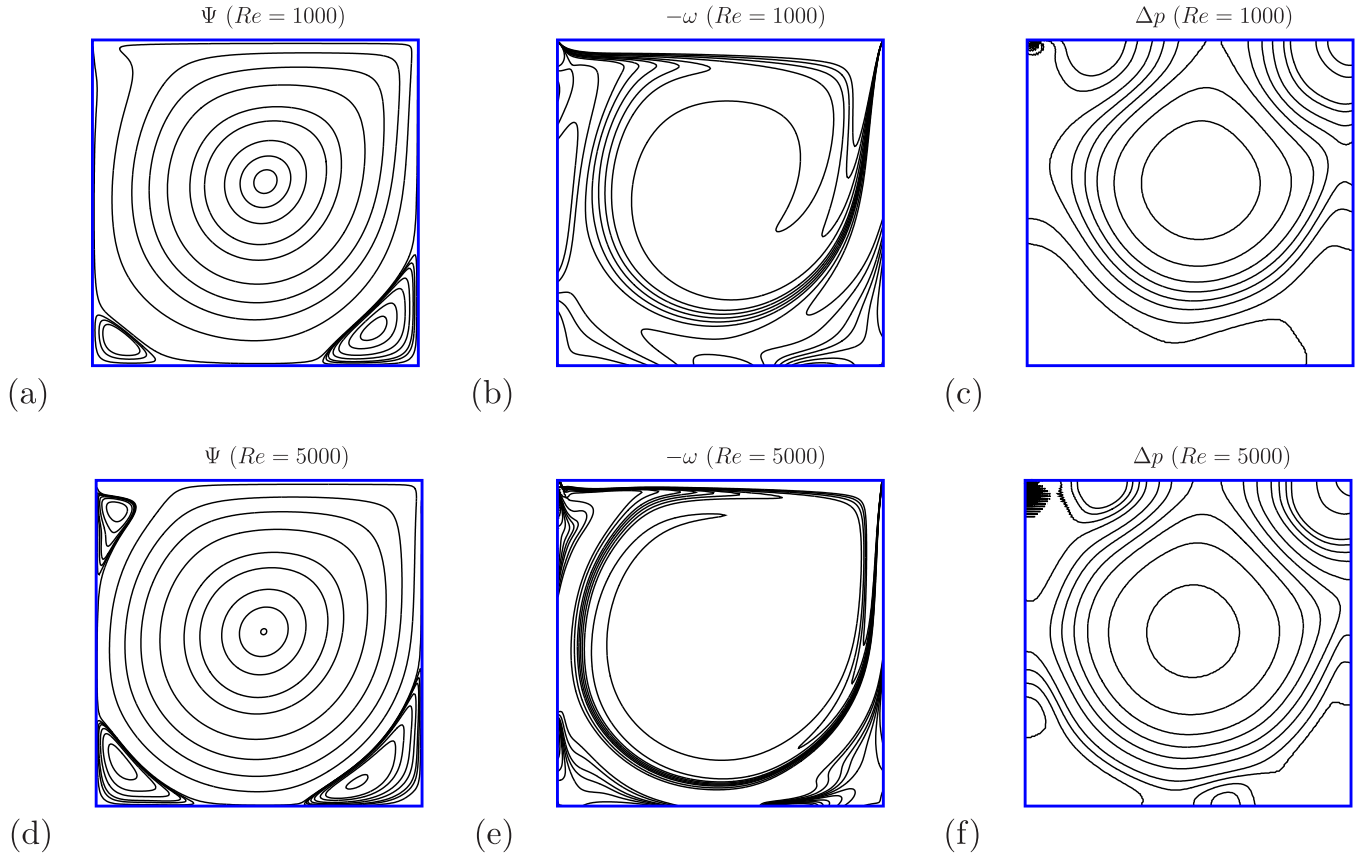


FIG. 8. Contour plots of the stream function  $\Psi$  (a), (d), the vorticity  $-\omega$  (b), (e) and the pressure deviation  $\Delta p$  (c), (f) at steady state for the 2D driven cavity at  $Re = 1000$  (upper row) and  $5000$  (lower row) obtained by the present SMAMEs simulations with  $N_L = 256$  and  $c = 50$ . The blue lines represent the wall boundaries.

using the vorticity-stream function formulation and have been widely used for benchmarking purposes. The data from [39] were obtained by a special formulation of the LBM using nonuniform meshes. It is seen that the present results are in good agreement with both reference results. The results for other low  $Re$  cases also agree well with the reference ones, but for conciseness they are not shown here.

In addition to the one-dimensional velocity profiles at the centerlines, we also looked into the 2D fields of the stream function  $\Psi$ , the vorticity  $\omega$ , and the pressure deviation  $\Delta p$  for the 2D cases. In two dimensions, the velocity is related to the stream function as  $u = \partial_y \psi$  and  $v = -\partial_x \psi$ . Once the velocity field is known,  $\Psi$  can be found through integration. As the pressure field was not given in Ref. [38], we also

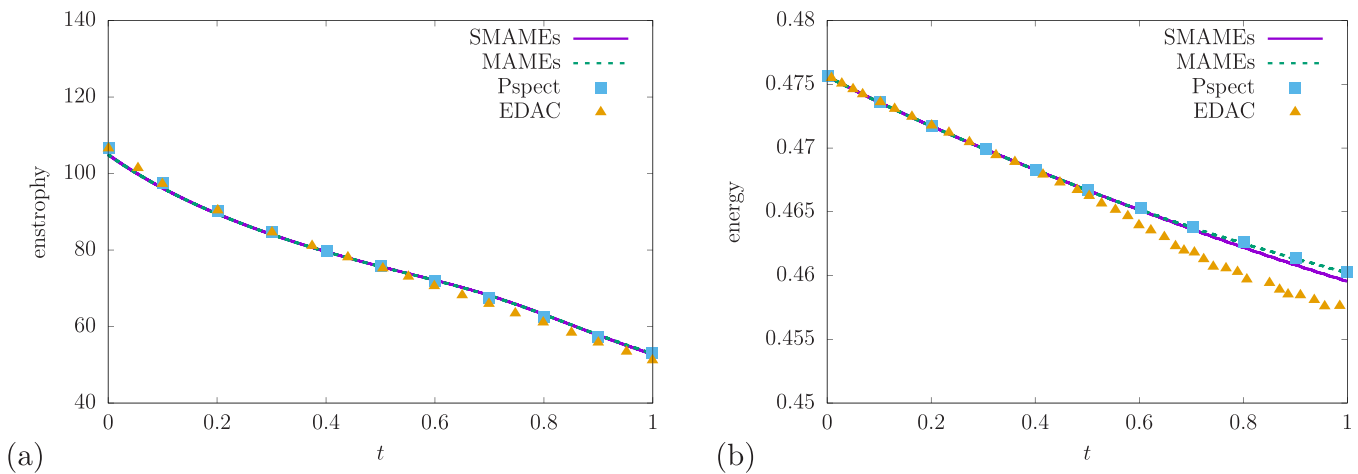


FIG. 9. Evolutions of (a) the total enstrophy and (b) the total kinetic energy for the doubly periodic shear layer at  $Re = 10000$ . The present simulation parameters are  $N_L = 320$ ,  $N_t = 16000$  ( $c = 50$ ). For the EDAC results from [14],  $N_L = 512$  and  $N_t = 5120$  ( $c = 10$ ). Note that "Pspect" denotes the results obtained by a pseudospectral solve on a  $768 \times 768$  grid [14,41].

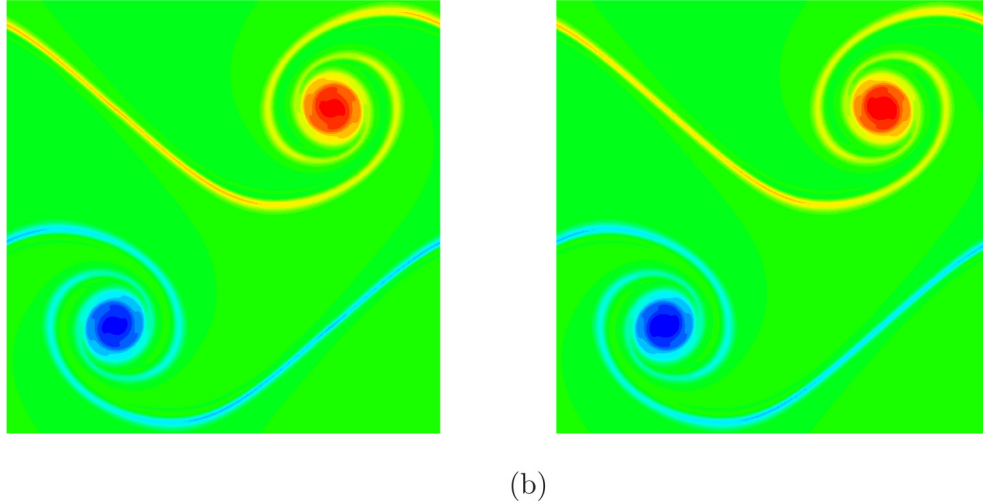


FIG. 10. The vorticity at  $t = 1.0$  for the doubly periodic shear layer at  $\text{Re} = 10\,000$  (a) by the present simulation using SMAMEs and (b) by using the original MAMEs. The simulation parameters are  $N_L = 320$ ,  $N_r = 16\,000$  ( $c = 50$ ).

examined another study of the 2D driven cavity by the LBM [40]. To compare the pressure deviation with those in Fig. 5 of [40],  $\Delta p$  is calculated as  $\Delta p = 10(p - p_0)/(\rho_r' U_{\text{lid},LU}^2)$  where  $\rho_r' = 1/2.7$  is the reference density used in Ref. [40],  $U_{\text{lid},LU} = U_{\text{lid}}/c = 1/c$  is the lid velocity in lattice unit, and  $p_0 = \rho_0 c_s^2 \approx 0.333333$  is the present initial pressure. Figure 8 gives the contour lines of  $\Psi$ ,  $-\omega$  and  $\Delta p$  when the flow becomes steady at  $\text{Re} = 1000$  and  $\text{Re} = 5000$ . The values for  $\Psi$  are  $-0.11745$ ,  $-0.115$ ,  $-0.11$ ,  $-0.1$ ,  $-0.09$ ,  $-0.07$ ,  $-0.05$ ,  $-0.03$ ,  $-0.01$ ,  $-10^{-4}$ ,  $10^{-5}$ ,  $5 \times 10^{-5}$ ,  $10^{-4}$ ,  $5 \times 10^{-4}$ ,  $10^{-3}$ ,  $1.5 \times 10^{-3}$ , and  $3 \times 10^{-3}$ , which were also used in Fig. 3 of [38] (except that  $-0.11745$  was replaced by  $-0.1175$  therein). The values for  $-\omega$  are  $-3$ ,  $-2$ ,  $-1$ ,  $-0.5$ ,  $0$ ,  $0.5$ ,  $1$ ,  $2$ ,  $3$ ,  $4$ , and  $5$  (same as those used in Fig. 4 of [38]). Note that there is a sign change in the vorticity when compared to [38]. The values for the pressure deviation  $\Delta p$  are  $5.0$ ,  $3.0$ ,  $1.0$ ,  $0.7$ ,  $0.3$ ,  $0$ ,  $-0.3$ ,  $-0.6$ ,  $-1.0$ ,  $-1.5$  in Fig. 8(c) for  $\text{Re} = 1000$ , and  $5.0$ ,  $2.5$ ,  $1.4$ ,  $1.2$ ,  $0.958$ ,  $0.7$ ,  $0.3$ ,  $0$ ,  $-0.3$ ,  $-0.6$ ,  $-1.0$ ,

$-1.5$  in Fig. 8(f) for  $\text{Re} = 5000$  which are the same as those labeled in Fig. 5 of [40] (except that  $0.958$  was replaced by  $1.0$  for  $\text{Re} = 5000$  therein). One can find that the present results are quite similar to Fig. 3 and 4 of [38] (for  $\Psi$  and  $-\omega$ ) and Figs. 1, 4, and 5 of [40] (for  $\Psi$ ,  $-\omega$ , and  $\Delta p$ ) at both  $\text{Re} = 1000$  and  $5000$ . At  $\text{Re} = 5000$ , the three eddies at the left-upper, left-lower, and right-lower corners are all well captured by the present simulation. This demonstrates the capability of the proposed SMAMEs to reproduce accurate results over the whole domain.

### C. Doubly periodic shear layer

The third case is the doubly periodic shear layer in two dimensions. The domain is a square  $[0, 1] \times [0, 1]$  with periodic boundary conditions in both the  $x$  and  $y$  directions. The initial

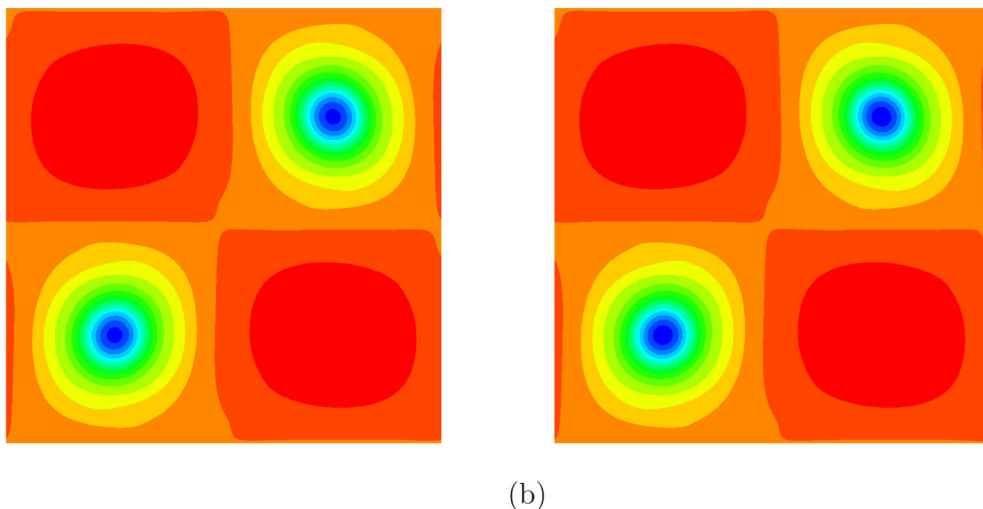


FIG. 11. The pressure at  $t = 1.0$  for the doubly periodic shear layer at  $\text{Re} = 10\,000$  (a) by the present simulation using SMAMEs and (b) by using the original MAMEs. The simulation parameters are the same as in Fig. 10.

TABLE III. Comparison of the average Nusselt numbers, the maximum  $u$  and its location in the  $y$  direction along the vertical centerline  $x = 0.5L_x$ , and the maximum  $v$  and its location in the  $x$  direction along the horizontal centerline  $y = 0.5L_y$  in steady state by the present SMAMEs simulations with those from [21,43] (in parentheses).

Ra	$10^3$	$10^4$	$10^5$	$10^6$
$\overline{Nu}$	1.118 (1.118)	2.245 (2.245)	4.528 (4.523)	8.851 (8.835)
$u_{\max}/V_{\text{diff}}$	3.644 (3.649)	16.185 (16.176)	34.907 (34.741)	65.065 (64.841)
$y_{\max}$	0.815 (0.815)	0.823 (0.826)	0.857 (0.855)	0.853 (0.852)
$v_{\max}/V_{\text{diff}}$	3.701 (3.698)	19.643 (19.624)	68.600 (68.619)	220.908 (220.438)
$x_{\max}$	0.175 (0.180)	0.117 (0.120)	0.063 (0.067)	0.037 (0.039)

density and velocity fields are given by

$$d(x, y, 0) = 1.0, \tag{35a}$$

$$u(x, y, 0) = \begin{cases} \tanh[\delta_w(y - 0.25)] & \text{if } y \leq 0.5, \\ \tanh[\delta_w(0.75 - y)] & \text{if } y > 0.5, \end{cases} \tag{35b}$$

$$v(x, y, 0) = \delta_p \sin[2\pi(x + 0.25)], \tag{35c}$$

where  $\delta_w = 80$  and  $\delta_p = 0.05$  are two parameters related to the width of the shear layer and the initial perturbation amplitude. The Reynolds number is taken to be  $Re = 10\,000$ .

The simulation is performed from  $t = 0$  to 1 by using the present SMAMEs and also the original MAMEs in Ref. [8]. Figure 9 shows the evolutions of the total enstrophy and kinetic energy [see Eq. (30) for their calculation] by using the SMAMEs, the MAMEs and some reference results from [14,41] (using the EDAC and pseudospectral methods, respectively). Overall, the present results on a  $320 \times 320$  grid are in good agreement with the pseudospectral results obtained on a much finer ( $768 \times 768$ ) grid. For the enstrophy, both the results by the SMAMEs and MAMEs agree very well with the pseudospectral results (one can hardly see any differences

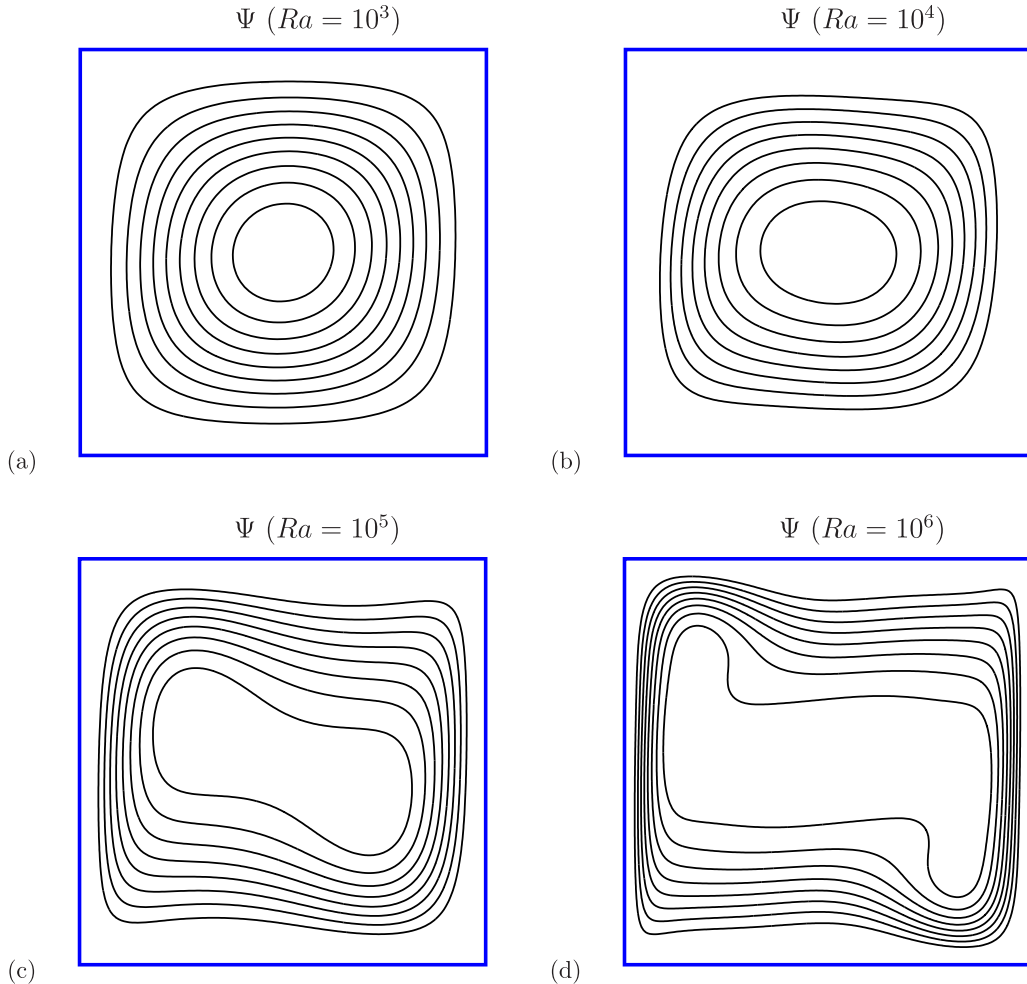


FIG. 12. Contour plots of the stream function for the 2D natural convection in a square cavity in steady state at different Rayleigh numbers: (a)  $Ra = 10^3$ , (b)  $Ra = 10^4$ , (c)  $Ra = 10^5$ , (d)  $Ra = 10^6$ , and  $Pr = 0.71$ . The shared parameter is  $c = 20$  and other simulation parameters are  $N_L = 100$  for  $Ra = 10^3$ ,  $N_L = 150$  for  $Ra = 10^4$  and  $10^5$ , and  $N_L = 200$  for  $Ra = 10^6$ . The blue lines represent the wall boundaries.

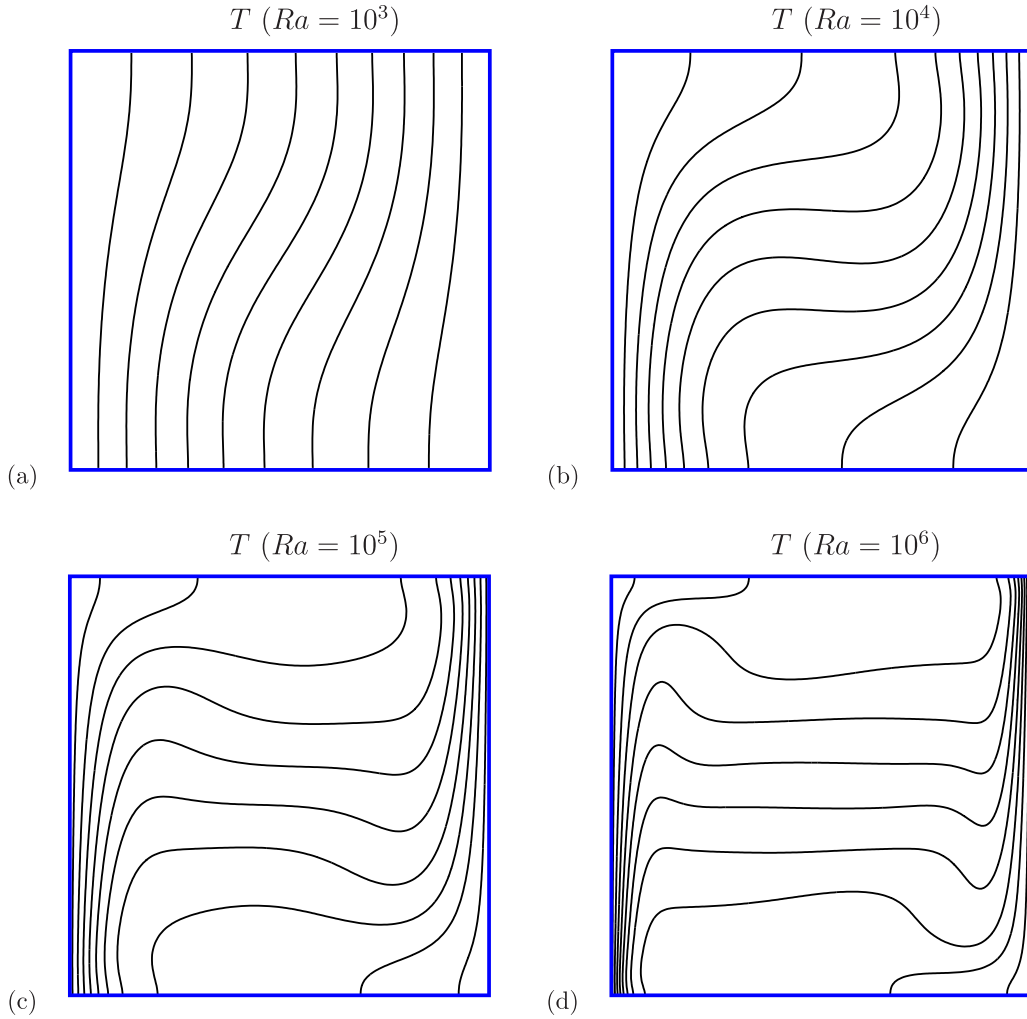


FIG. 13. Contour plots of the temperature for the 2D natural convection in a square cavity in steady state at different Rayleigh numbers: (a)  $Ra = 10^3$ , (b)  $Ra = 10^4$ , (c)  $Ra = 10^5$ , (d)  $Ra = 10^6$ , and  $Pr = 0.71$ . The simulation parameters are the same as in Fig. 12.

between them from Fig. 9) For the kinetic energy, the evolution by the MAMEs match the pseudospectral results slightly better than that by the SMAMEs. In addition, Figs. 10 and 11 show the contours of the vorticity and the pressure at  $t = 1$  by the present simulation and by the MAMEs. One can see that the two sets of results look similar to each other, and that the curled shear layers still look smooth and there are no spurious vortices. Due to the simplified formulation and implementation, the present simulation only takes about 258.6 s, whereas that using the original MAMEs takes 365.5 s on the same computer under the same settings. That means the present method saves about 30% computation time compared with the original method using the MAMEs. It is noted that the present simulation is unstable when the mesh is too coarse. Even on a  $256 \times 256$  grid the simulation blew up (the simulation using the MAMEs was not stable either). Previously, it was found that some more robust upwind methods can keep the simulation at such a high Re stable on a coarse grid. However, they often produce spurious vorticities under such situations [41]. The present method using the SMAMEs has low tolerance to the underresolved situations. On the other hand, it is less likely to produce spurious vortices and unphysical results.

#### D. Natural convection in a square cavity in two dimensions

The next problem is the 2D natural convection in a square cavity which involves heat conduction. This is a canonical benchmark problem for incompressible thermal flows and has been investigated by various numerical methods (including the LBM) [21–23,42,43]. The domain is a rectangle  $[0, L_x] \times [0, L_y]$  enclosed by four stationary solid walls. Both the width  $L_x$  and height  $L_y$  of the cavity are equal to  $H$ , which is chosen as the characteristic length. The velocities at the four wall boundaries are all zero ( $u = v = 0$ ). The left wall is maintained at a high temperature  $T_h$  and the right wall is kept at a low temperature  $T_l$ , giving a temperature difference  $\Delta T = T_h - T_l$ . The upper and lower walls are both adiabatic (i.e., have zero normal heat flux or  $\partial_y T = 0$ ). The characteristic velocity is chosen as  $U_r = \sqrt{\beta \Delta T g H}$ . The Rayleigh number is given by  $Ra = g \beta \Delta T H^3 / (\nu^2 / Pr)$ . The Reynolds number is given by  $Re = U_r H / \nu$  and related to Ra as  $Re = \sqrt{Ra / Pr}$ . Without loss of generality, we use  $T_h = 1$  and  $T_l = 0$ , thus the temperature difference is  $\Delta T = 1$  and the average temperature is  $T_0 = 0.5$ . The initial fields are set to be  $u = v = 0$ ,  $\rho = 1$  and  $T = 0$ . After certain time, the flow and temperature fields inside the cavity achieve a steady state which

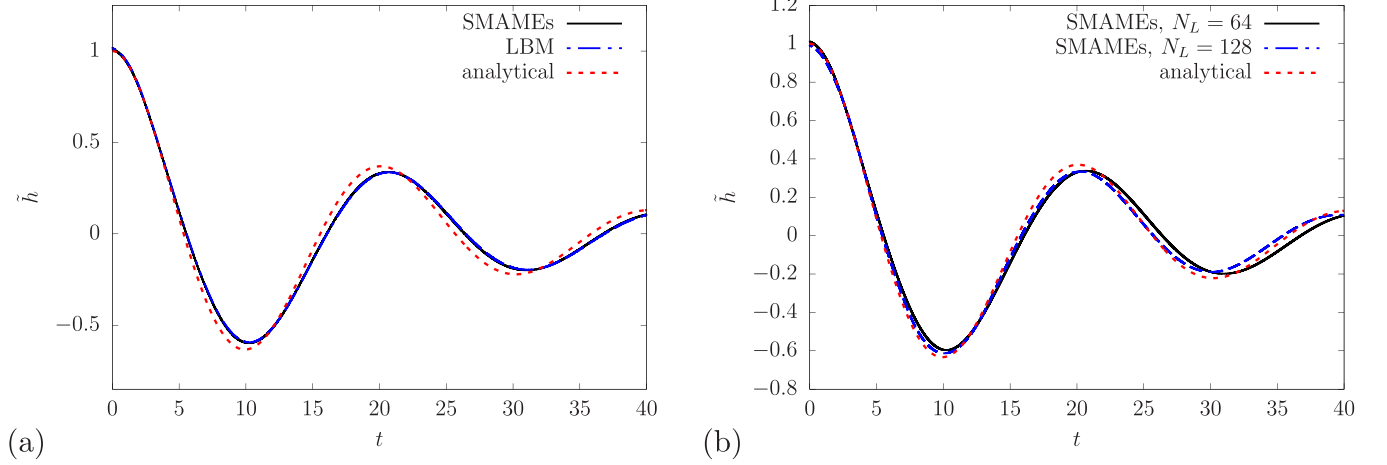


FIG. 14. Evolutions of the (scaled) interface displacement at the left boundary for the capillary wave at  $Re = 1000$ . In both (a) and (b) the dashed line is the analytical prediction by Eq. (39). In (a) the solid line is by the present method, and the dash-dotted line is by the MRT-LBM. In (b) the solid line is obtained at  $N_L = 64$ , and the dash-dotted line,  $N_L = 128$ . The shared simulation parameters in (a) are  $N_L = 64$ ,  $N_t = 384$  ( $c = 6$ ),  $Cn = 0.0625$ ,  $Pe = 2 \times 10^4$ . For the fine mesh solution in (b),  $N_t = 3072$  ( $c = 24$ ),  $Cn = 0.03125$ ,  $Pe = 2 \times 10^4$ .

is determined by the criteria  $\max ||\mathbf{u}|^{n+1} - |\mathbf{u}|^n|/U_r < 10^{-8}$  and  $\max |T^{n+1} - T^n|/\Delta T < 10^{-8}$  (i.e., the scaled changes in the velocity magnitude and the temperature between two consecutive steps are both less than  $10^{-8}$  everywhere). For this problem, the average Nusselt number is computed as  $\overline{Nu} = Q/Q_c$  where

$$Q = \int_0^{L_x} \int_0^{L_y} q_x(x, y) dy dx, \quad (36)$$

is the actual heat flux across the cavity and

$$Q_c = (\rho_0 v / Pr) [(T_h - T_l) / L_x] L_y, \quad (37)$$

is the heat flux if there was only pure conduction [21]. The local heat flux in the  $x$  direction  $q_x$  is calculated as [23]

$$q_x(x, y) = uT(x, y) - (v/Pr)\partial_x T(x, y). \quad (38)$$

In addition to  $\overline{Nu}$ , the maximum  $u$  along the vertical centerline  $x = 0.5L_x$  and the maximum  $v$  along the horizontal centerline  $y = 0.5L_y$  were also extracted.

Four cases at  $Ra = 10^3, 10^4, 10^5$ , and  $10^6$  were simulated by the present SMAMEs coupled with the temperature evolution equation, Eq. (14). The Prandtl number is fixed at  $Pr = 0.71$ . The common numerical parameter is  $c = 20$  and other simulation parameters are  $N_L = 100$  for  $Ra = 10^3$ ,  $N_L = 150$  for  $Ra = 10^4$  and  $10^5$ , and  $N_L = 200$  for  $Ra = 10^6$ . Table III shows the average Nusselt numbers and the maximum velocities and their locations along the centerlines in steady

state for the four cases obtained by the present simulations using the SMAMEs, together with the reference results from [21,43]. Note that the reference values in the brackets are from Table III (a, b, d, finest grid) of [21] (for  $Ra = 10^4, 10^5$  and  $10^6$ ) and from Table 1 (two-layer approach, finest grid) of [43] (for  $Ra = 10^3$ ). To facilitate the comparison with previous studies,  $u_{max}$  and  $v_{max}$  in Table III are scaled by the diffusion velocity  $V_{diff} = v/(PrL_x)$  (instead of  $U_r$ ). It is seen that the present results are in good agreement with the reference ones for all cases. Figures 12 and 13 show the streamlines and the isotherms inside the cavity for the four cases, respectively. All of them are quite similar to previous results by other methods (e.g., see Fig. 9 of [21] and Figs. 3 and 4 of [42]).

### E. Capillary wave in 2D

Next, we study some more complicated two-phase flows using the CHE for interface capturing. Besides, the surface tension effects are taken into account in the momentum equations. For such problems, there are additional parameters: (1) the Cahn number  $Cn = W/L_c$  (i.e., the interface thickness measured by the characteristic length) and (2) the Peclet number  $Pe = U_c L_c^2 / (M\sigma)$  (reflecting the relative importance of convection over diffusion in the CHE). For two-phase flows one can derive a velocity scale from the surface tension and viscosity as  $\sigma / (\rho_0 v)$ , and it is chosen to be the default characteristic velocity  $U_c$ . From  $U_c$  one can derive a characteristic time as  $T_c = L_c / U_c$ . For two-phase problems, the above  $U_c$  and  $T_c$  are used to scale the velocity and time (unless specified otherwise).

The first two-phase problem is the 2D capillary wave. The domain is a square  $[0, 1] \times [0, 1]$  ( $L_c$  is set to the side length  $L = L_x = L_y$ ). The left and right boundaries are periodic, and the top and bottom boundaries are no-slip walls. The upper half domain is filled with the “red” fluid where  $\phi = 1$  and the lower is filled with the “blue” fluid where  $\phi = -1$  (note that the two fluids have the same density and viscosity, thus are completely symmetric; for convenience we denote them as “red” and “blue”). The initial interface

TABLE IV. Comparisons of the oscillation period for the capillary wave at  $Re = 1000$  and  $4000$ . The shared simulation parameter is  $Pe = 2 \times 10^4$ . The Cahn numbers are  $Cn = 0.0625$  for  $N_L = 64$  and  $Cn = 0.03125$  for  $N_L = 128$ .

Reynolds number	1000	4000
Period (analytical)	20.071	38.751
Period   Error ( $N_L = 64, c = 6$ )	20.669   2.98%	40.089   3.45%
Period   Error ( $N_L = 128, c = 24$ )	20.265   0.97%	39.293   1.40%

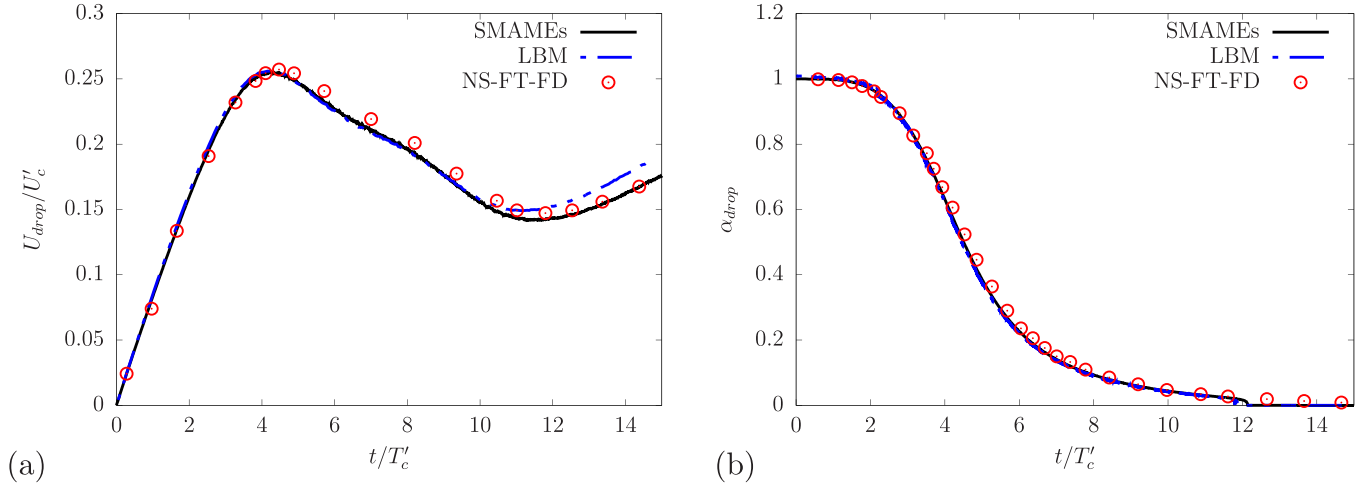


FIG. 15. Evolutions of (a) the centroid velocity  $U_{\text{drop}}$  in the axial direction and (b) the aspect ratio  $\alpha_{\text{drop}}$  of the drop at  $\text{Eo} = 144$  and  $\text{Oh} = 0.0466$  for the falling drop problem by the present method, by the axisymmetric LBM in Ref. [28] and by the finite difference solution of the NSEs and the front-tracking method [46]. The present simulation parameters are  $N_L = 50$ ,  $N_t = 4000$  ( $c = 80$ ),  $\text{Cn} = 0.06$ , and  $\text{Pe} = 1000$ .

is slightly perturbed with the interface position varying with  $x$  as  $h(x) = h_{eq} + A_p \cos[k(x + 0.5)]$ , where  $h_{eq} = 0.5$  is the equilibrium interface position,  $A_p = 0.01$  is the amplitude of disturbance and  $k = 2\pi/\lambda$  is the wave number ( $\lambda = L_x = 1$  is the wavelength). The initial order parameter field is set to  $\phi(x, y, 0) = \tanh\{2[y - h(x)]/\text{Cn}\}$ . The interface position  $h_0(t)$  at  $x = 0$  was monitored during the simulation. The Reynolds number is defined as  $\text{Re} = U_c L_c / \nu = \sigma L_c / (\rho_0 \nu^2)$ . The case at  $\text{Re} = 1000$  was first investigated. For this problem, there exists a basic frequency  $\omega_0 = \sqrt{\sigma k^3 / (2\rho_0)}$ . When both the liquid and gas have the same the kinematic viscosity ( $\nu$ ) and the perturbation is small ( $A_p \ll 1$ ), one can obtain the analytical solution for this problem [44,45],

$$\tilde{h}(t) = \frac{h_{eq} - h_0(t)}{A_p} = \sum_{i=1}^4 \frac{z_i \omega_0^2}{Z_i (z_i^2 - \bar{\epsilon} \omega_0)} \times \exp\left[\frac{(z_i^2 - \bar{\epsilon} \omega_0)t'}{\omega_0}\right] \text{erfc}\left(z_i \sqrt{\frac{t'}{\omega_0}}\right), \quad (39)$$

where  $t' = \omega_0 t$  and  $\bar{\epsilon} = \nu k^2 / \omega_0$  are the scaled time and dimensionless viscosity,  $z_i$  are the four roots of the algebraic equation  $z^4 - \sqrt{\bar{\epsilon} \omega_0} z^3 - \bar{\epsilon} \omega_0 z^2 + (\bar{\epsilon} \omega_0)^{3/2} z + \omega_0^2 = 0$  and  $Z_1 = (z_2 - z_1)(z_3 - z_1)(z_4 - z_1)$ ,  $Z_2 = (z_3 - z_2)(z_4 - z_2)(z_1 - z_2)$ ,  $Z_3 = (z_4 - z_3)(z_1 - z_3)(z_2 - z_3)$ ,  $Z_4 = (z_1 - z_4)(z_2 - z_4)(z_3 - z_4)$ . Figure 14(a) shows the evolutions of  $\tilde{h}$  over  $0 \leq t \leq 40$  by the present method and the MRT-LBM using the same numerical parameters  $N_L = 64$ ,  $N_t = 384$  ( $c = 6$ ). It is seen that the present numerical results are very close to (almost overlap) that by the MRT-LBM. Both numerical solutions agree with the analytical one in the early stage and the deviations increase gradually with time. After about two oscillation periods, the deviations remain to be small and can actually be reduced by increasing the resolution in space and time. This is observed from Fig. 14(b) which also shows the results obtained by the present method using a finer mesh with  $N_L = 128$ ,  $N_t = 3072$  ( $c = 24$ ). Besides, another case at an even higher  $\text{Re} (=4000)$  was studied. Table IV compares the oscillation periods obtained by the present

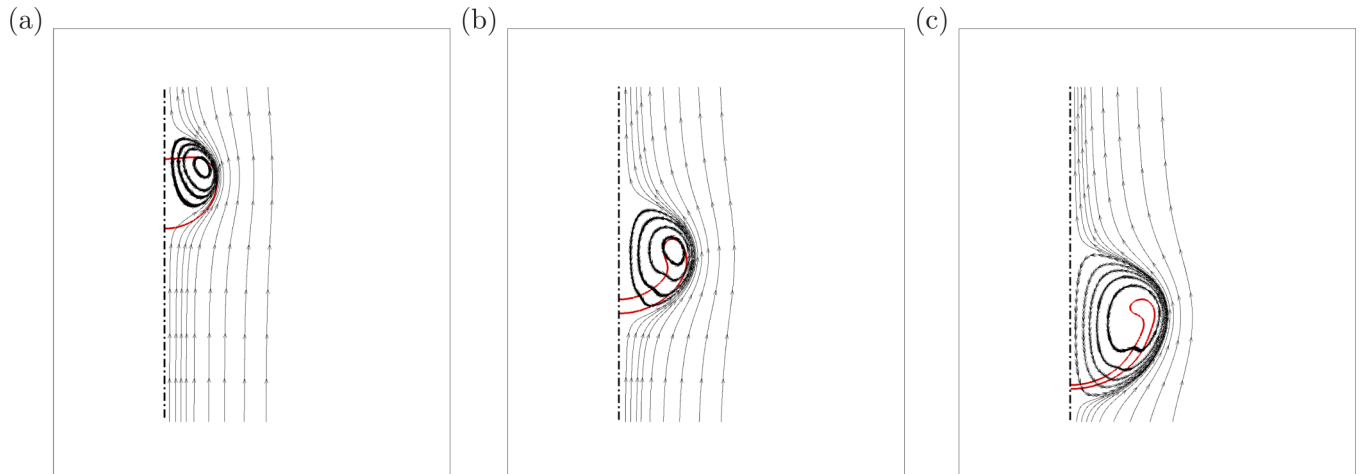


FIG. 16. Snapshots of the drop interfaces (red lines) and the stream traces around the drop (in the frame moving with the drop) at three selected times with an interval  $\Delta t/T'_c = 3.873$  (a)  $t/T'_c = 3.873$ , (b)  $t/T'_c = 7.746$ , (c)  $t/T'_c = 11.619$  at  $\text{Eo} = 144$ ,  $\text{Oh} = 0.0466$ ,  $r_\rho = 1.15$ , and  $r_\eta = 1$ . The dash-dotted line is the  $z$  axis. The simulation parameters are as in Fig. 15.

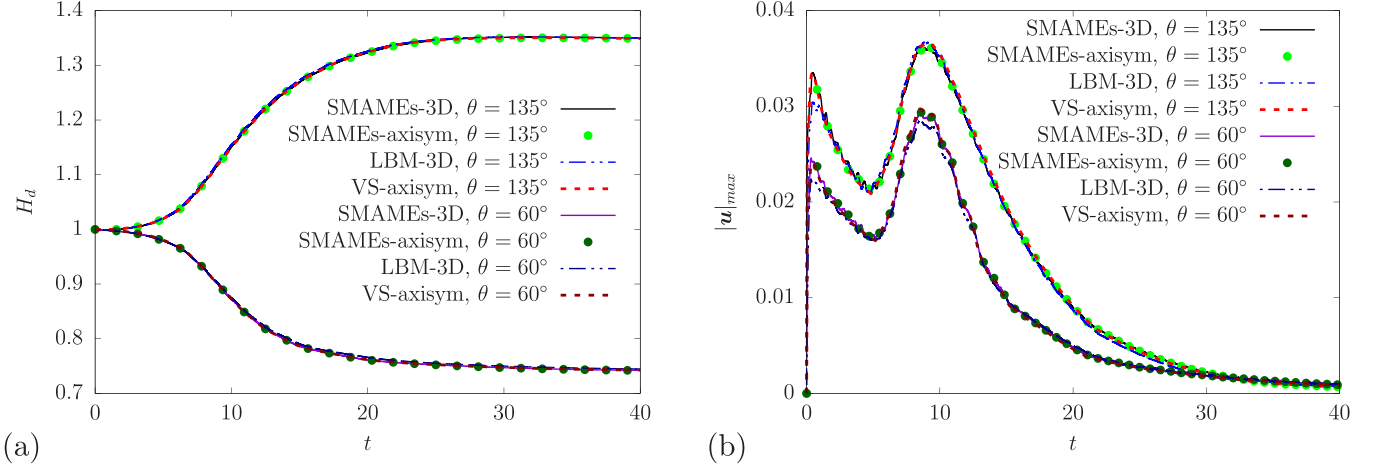


FIG. 17. Evolutions of (a) the droplet height  $H_d$  (b) the maximum velocity magnitude  $|\mathbf{u}|_{\max}$  during the drop dewetting/spreading computed by three different methods. The solid lines are by the present 3D simulations, the filled circles are by the present axisymmetric simulations, the dash-dot-dot lines are by the 3D LBM using the weighted MRT collision model [32] and the dashed lines are by the axisymmetric simulation using the VS formulation [47]. The shared simulation parameters are  $N_L = 32$ ,  $N_r = 320$  ( $c = 10$ ),  $Cn = 0.1$ , and  $Pe = 8000$ .

simulations using two sets of meshes with the analytical periods for the two cases. It is seen that under all situations the deviations in the period are small (less than 5%), and as the grid is refined ( $N_L$  is changed from 64 to 128) the deviations decrease quickly to around 1%. Finally, it is noted that different values of  $N_r(c)$  were tested for the case at  $Re = 1000$  with  $Cn = 0.0625$  and  $Pe = 2 \times 10^4$ . When  $c$  further increases (to 10 and 20), the results are almost the same as that obtained with  $c = 6$ . When  $c$  decreases to 5, the simulation becomes unstable no matter whether the present SMAMEs or the LBM is used. The reason is likely to be that for two-phase flows the CHE for interface evolution may impose an even more stringent condition on the time step. Under such situations, the present method should be as robust as the LBM with regard to the stability issue. At the same time, it is much easier to implement and performs faster. Therefore, overall the present method can be more competitive than the LBM for two-phase flows.

### F. Falling drop

The second two-phase problem is a falling drop under the action of a body force. This problem is symmetric about the  $z$  axis and can be simplified to an axisymmetric problem. Previously, it was studied by an axisymmetric LBM in Ref. [28] and by a finite difference front tracking method in Ref. [46] that solves the incompressible NSEs. In this problem, a drop is surrounded by the ambient gas. The drop/gas density ratio is  $r_\rho = \rho_L/\rho_G = 1.15$  ( $\rho_L$  and  $\rho_G$  are the densities of the liquid and gas) and the dynamic viscosity ratio is  $r_\eta = \eta_L/\eta_G = 1$  ( $\eta_L$  and  $\eta_G$  are the dynamic viscosities of the liquid and gas). The drop radius  $R$  is chosen as the characteristic length ( $L_c = R$ ). The domain is a rectangle  $[0, 24] \times [0, 8]$  ( $L_z = 24$  and  $L_r = 8$ ). Symmetric boundary conditions are applied on the boundary  $r = 0$  and no slip wall boundary conditions are used for the other three boundaries. The initial drop center is located at  $(z_c, r_c) = (2, 0)$ . The order parameter field is initialized to be  $\phi(z, r, 0) = -\tanh[2(r_{dc} - R)/Cn]$  where  $r_{dc} = \sqrt{(z - z_c)^2 + (r - r_c)^2}$ . The body force

of magnitude  $g$  is applied along the  $z$  direction. Note that with some manipulation of the pressure, the body force may be applied only on the drop [1]. Two main dimensionless parameters are the Eotvos number and Ohnesorge number defined as

$$Eo = \frac{g(\rho_L - \rho_G)D^2}{\sigma}, \quad Oh = \frac{\eta_L}{\sqrt{\rho_L D \sigma}}, \quad (40)$$

where  $D = 2R$  is the drop diameter. They are set to  $Eo = 144$  and  $Oh = 0.0466$  (same as in Refs. [28,46]). To facilitate the comparison with previous results, we scale the velocity and time using  $U'_c = \sqrt{gD}$  and  $T'_c = \sqrt{D/g}$ . Because the density ratio is small, the Boussinesq approximation is used here (as in Ref. [28]), and the physical density is assumed to be unity for both fluids. To account for the density difference, one needs to multiply the body force acting on the drop by a factor  $(\rho_L - \rho_G)/[(\rho_L + \rho_G)/2] = 2(r_\rho - 1)/(r_\rho + 1)$  where  $(\rho_L + \rho_G)/2$  is the (real) average density of the two fluids (see the Appendix of [28]). During the simulation, we monitor the centroid velocity  $U_{\text{drop}}$  along the axial direction, the drop thickness (in the axial direction)  $Th_{\text{drop}}$  and the drop width (in the radial direction)  $Wh_{\text{drop}}$ . From the latter two, we calculate the aspect ratio of the drop as  $\alpha_{\text{drop}} = Th_{\text{drop}}/Wh_{\text{drop}}$ . The centroid velocity  $U_{\text{drop}}$  is calculated by  $U_{\text{drop}} = \int_{A|\phi>0} ru(r, z) dr dz / \int_{A|\phi>0} r dr dz$  where  $A|\phi>0$  represents the region where  $\phi > 0$ . Figure 15 shows the evolutions of the centroid velocity  $U_{\text{drop}}$  and the aspect ratio  $\alpha_{\text{drop}}$  of the drop obtained by the present method together with those from [28,46]. It is found that the present result follows the prediction by the axisymmetric LBM very well, and both of them are close to that by the front tracking method in Ref. [46] till  $t/T'_c \approx 12$ . After that, the front tracking method still predicts a nonzero drop thickness whereas the simulations using the phase field model (both the present and [28]) predict drop breakup. This is an inherent difference between the two types of methods. Besides the drop velocity and aspect ratio, we also examined the drop interface and the flow around the drop, as shown in Fig. 16. All of them are close to those by the axisymmetric LBM simulation (see Fig. 11

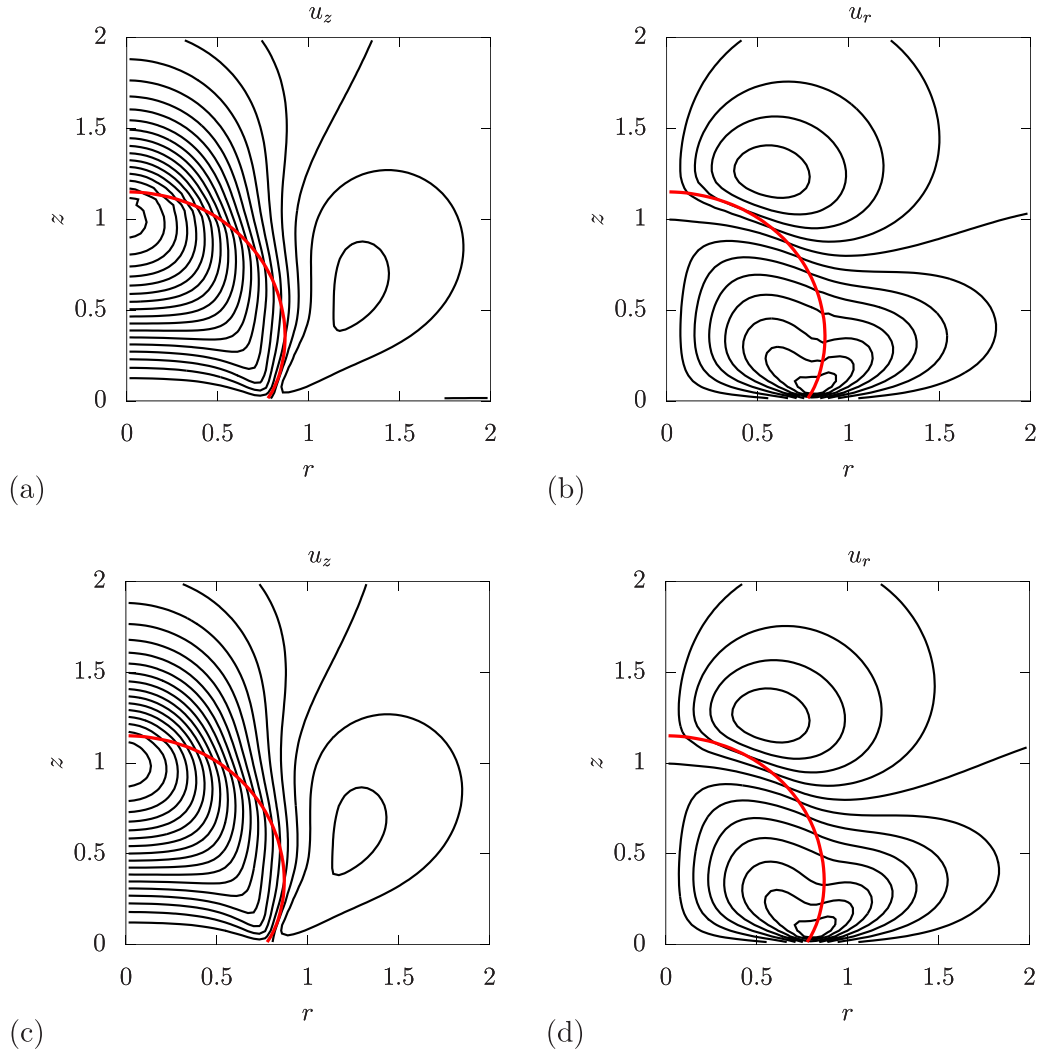


FIG. 18. Contour plots of the velocity components along the  $z$  axis and along the radial direction,  $u_z$  and  $u_r$ , at  $t = 10$  for axisymmetric drop dewetting on a hydrophobic wall. The physical parameters are  $Re = 100$  ( $Oh = 0.1$ ) and  $\theta = 135^\circ$ . The red lines represent the drop interfaces. The shared simulation parameters are  $N_L = 32$ ,  $N_r = 320$  ( $c = 10$ ),  $Cn = 0.1$ , and  $Pe = 8000$ . The upper row (a), (b) are the present results using the SMAMEs. The lower row (c), (d) are by the axisymmetric VS simulation in Ref. [47].

of [28]). The deformations of the drop at the three selected times are also in agreement with the front tracking results (see Fig. 2 of [46]).

### G. Drop spreading and dewetting on a wall

The third two-phase problem is on the motion of a drop on a wall with a contact angle  $\theta$ . Initially, the drop is a hemisphere with a radius  $R = 1$  (i.e., the characteristic length  $L_c = R$ ) and its center at  $(0,0,0)$ . The Ohnesorge number is given by  $Oh = \rho_0 v / \sqrt{\rho_0 R \sigma} = 1/\sqrt{Re}$ . Two cases with  $\theta = 135^\circ$  and  $60^\circ$  at  $Re = 100$  ( $Oh = 0.1$ ) were investigated. On the hydrophobic wall with  $\theta = 135^\circ$  the drop dewets from the wall whereas on the hydrophilic wall with  $\theta = 60^\circ$  the drop spreads on the wall. The domain size is a cube  $[-3, 3] \times [-3, 3] \times [0, 3]$ . Due to symmetry, the actual simulation domain was  $[0, 3] \times [0, 3] \times [0, 3]$ . Symmetric boundary conditions were applied on four side boundaries ( $x = 0, 3$  and  $y = 0, 3$ ), and no slip boundary conditions were used on the top and bottom boundaries ( $z = 0, 3$ ). This prob-

lem is actually symmetric about the  $z$  axis and may be also handled under the axisymmetric geometry. In the axisymmetric simulations using the SMAMEs, the domain is  $[0, 3] \times [0, 3]$  ( $L_z = 3$  and  $L_r = 3$ ). For the LBM simulations, the D3Q19 velocity model is used and the collision model is the weighted MRT [32]. Besides, axisymmetric simulations using the vorticity stream function (VS) formulation [47] were also performed. Unlike the artificial compressibility methods (e.g., LBM, MAMEs, or SMAMEs), the VS formulation solves the incompressible NSEs without any compressibility errors (it has to solve the Poisson-like equations). Two main quantities were monitored: the drop height (in the  $z$  direction)  $H_d$  and the maximum velocity magnitude  $|\mathbf{u}|_{\max}$  in the whole domain. Figure 17 shows the results by the four sets of simulations (the 3D and axisymmetric SMAMEs, 3D LBM and axisymmetric VS) for this problem using the same  $\delta_x$  and  $\delta_r$ . It is seen that for both cases at  $\theta = 135^\circ$  and  $60^\circ$  all the methods predict the evolutions of  $H_d$  and  $|\mathbf{u}|_{\max}$  to be quite close to each other. More careful examinations reveal that the present results by the SMAMEs are closer to those by the VS-based solver.

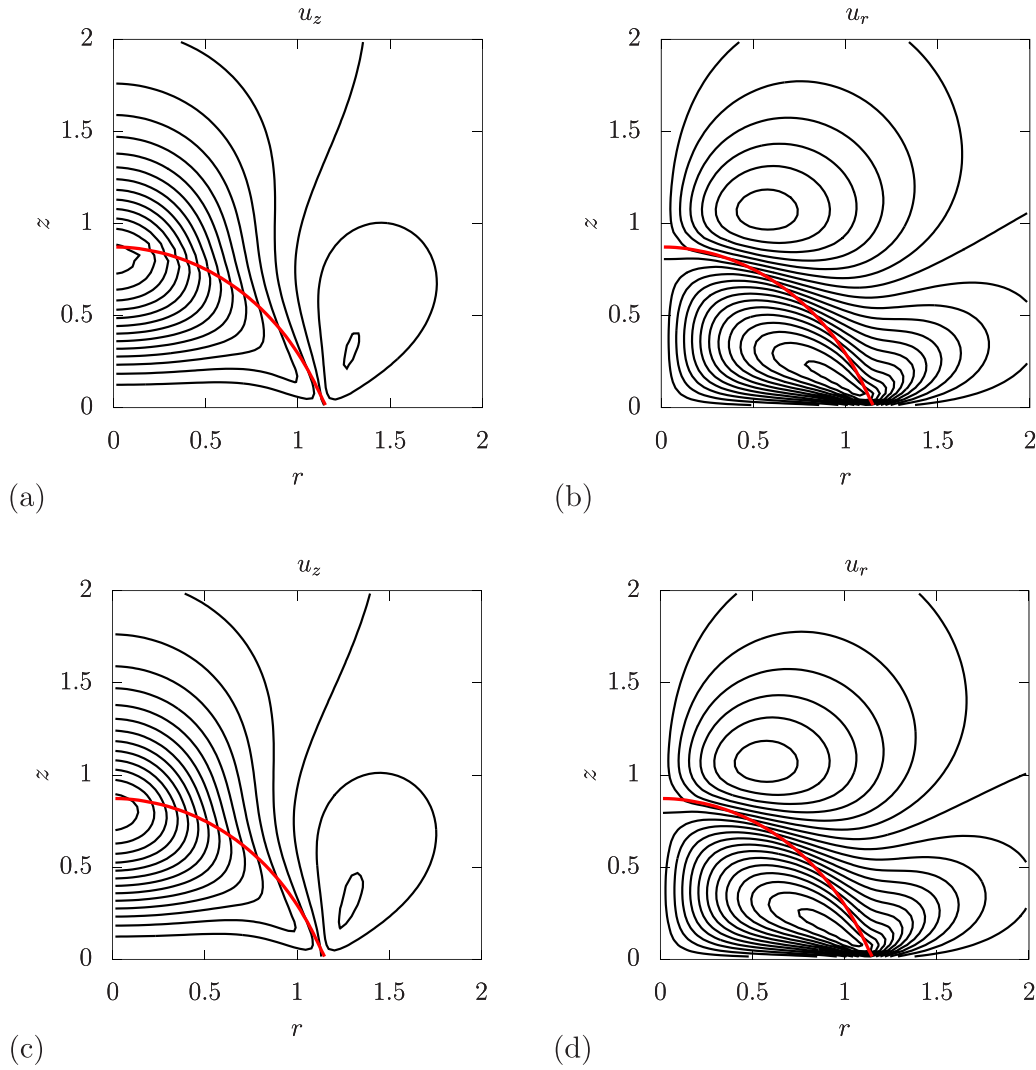


FIG. 19. Contour plots of the velocity components  $u_z$  and  $u_r$  at  $t = 10$  for axisymmetric drop spreading on a hydrophilic wall. The physical parameters are  $Re = 100$  ( $Oh = 0.1$ ) and  $\theta = 60^\circ$ . The red lines represent the drop interfaces. The simulation parameters are the same as those in Fig. 18. The upper row (a), (b) are the present results using the SMAMEs. The lower row (c), (d) are by the axisymmetric VS simulation in Ref. [47].

This could be attributed to the simplifications made in the present method which probably reduce the overall magnitude of the error terms. Besides the drop height and maximum velocity magnitude, we also examined the drop interface and the contour plots of the velocity components around the drop. Figure 18 shows the contour lines of the velocity components along the  $z$  axis ( $u_z$ ) and along the radial direction ( $u_r$ ) at  $t = 10$  in the axisymmetric simulation of drop dewetting by the SMAMEs and by axisymmetric VS formulation in Ref. [47]. Similar plots for axisymmetric drop spreading are given in Fig. 19. It is seen that the present results by the SMAMEs are quite similar to those by the axisymmetric VS simulations for both drop dewetting and spreading.

**H. Coalescence induced drop jumping on a nonwetting wall in three dimensions**

The last problem is on the coalescence induced drop jumping on a nonwetting wall (contact angle  $\theta = 180^\circ$ ) in three

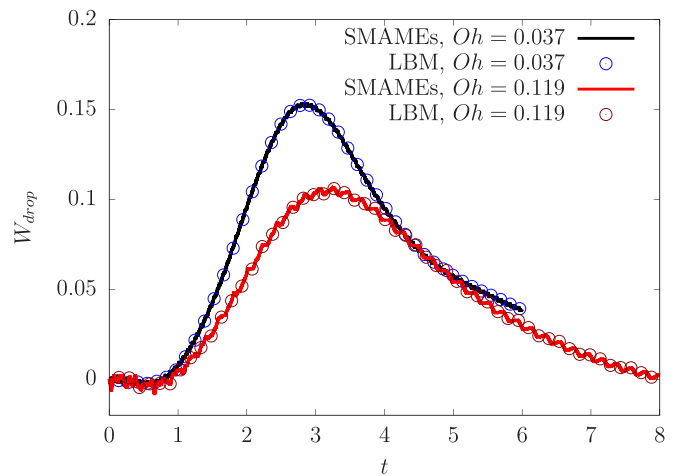


FIG. 20. Evolutions of the  $z$  component of the centroid velocity of the drop at  $Oh = 0.037$  and  $0.119$ . The shared simulation parameters are  $N_L = 40$ ,  $N_t = 400$  ( $c = 10$ ),  $Cn = 0.1$ ,  $Pe = 8 \times 10^3$ .

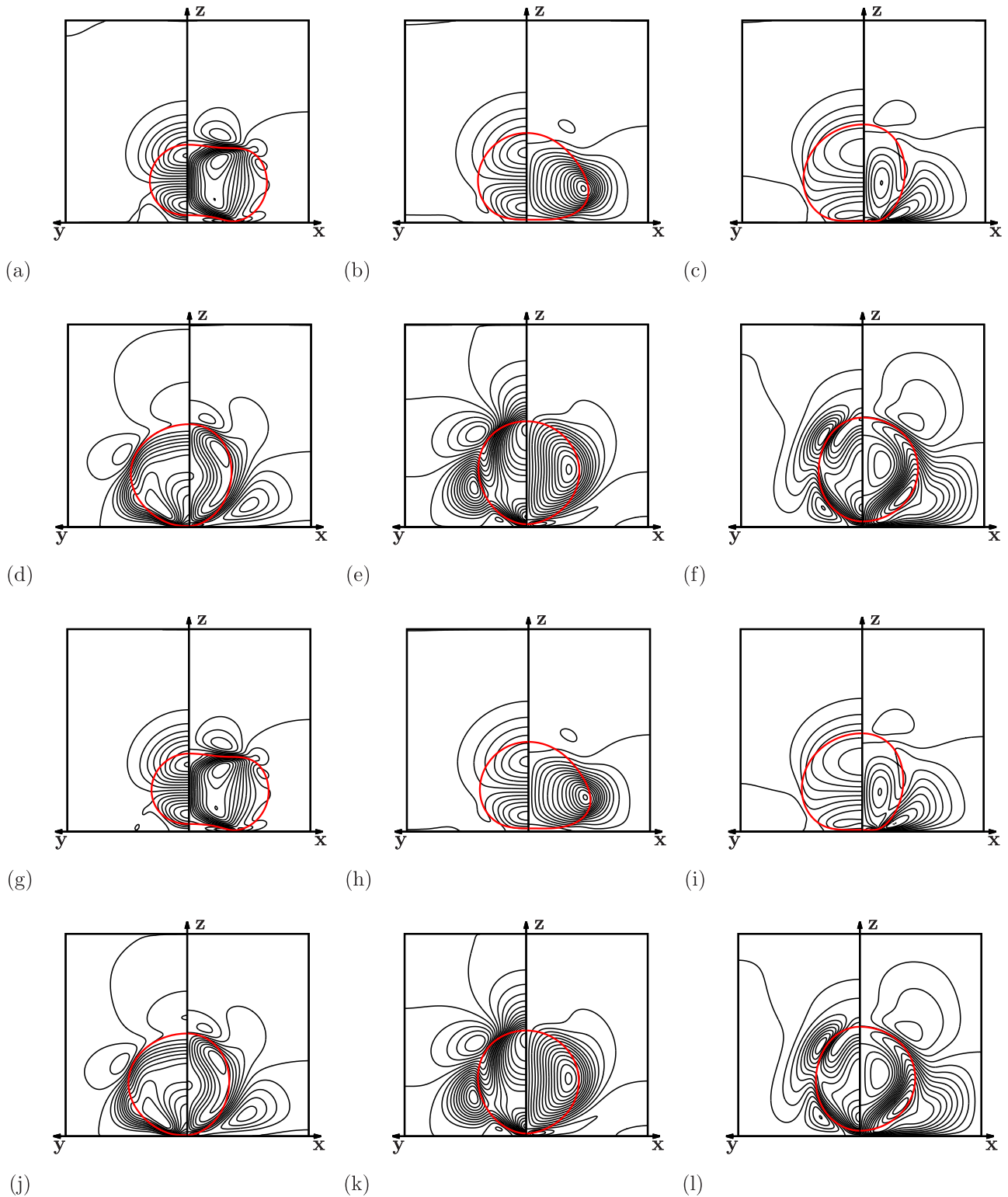


FIG. 21. Snapshots of the drop shapes (in red solid lines) and the contour plots of the velocity component  $u$  (in the middle  $x$ - $z$  plane) and  $v$  (in the middle  $y$ - $z$  plane) at  $t = 1.0, 2.0, 3.0, 4.0, 5.0,$  and  $6.0$  [(a)–(f) by the present SMAMEs simulation and (g)–(l) by the 3D MRT-LBM simulation] at  $Oh = 0.037$  for the coalescence induced drop jumping on a nonwetting wall. In each panel, the left part shows the middle  $y$ - $z$  plane at  $x = 0$  and the right shows the middle  $x$ - $z$  plane at  $y = 0$ . The shared simulation parameters are as in Fig. 20.

dimensions. The domain is a box  $[-3, 3] \times [-3, 3] \times [0, 5]$ . Initially there are two spherical drops having the same radius  $R$  (chosen as the characteristic length  $L_c$ ) and their centers are at  $(\pm 1, 0, 1)$ . They start to coalesce with each other and

interact with the nonwetting wall at the same time. Under certain conditions, the drop after coalescence may jump away from the wall [48]. Due to symmetry, the actual simulation domain was  $[0, 3] \times [0, 3] \times [0, 5]$  ( $L_x = L_y = 3$  and  $L_z = 5$ ).

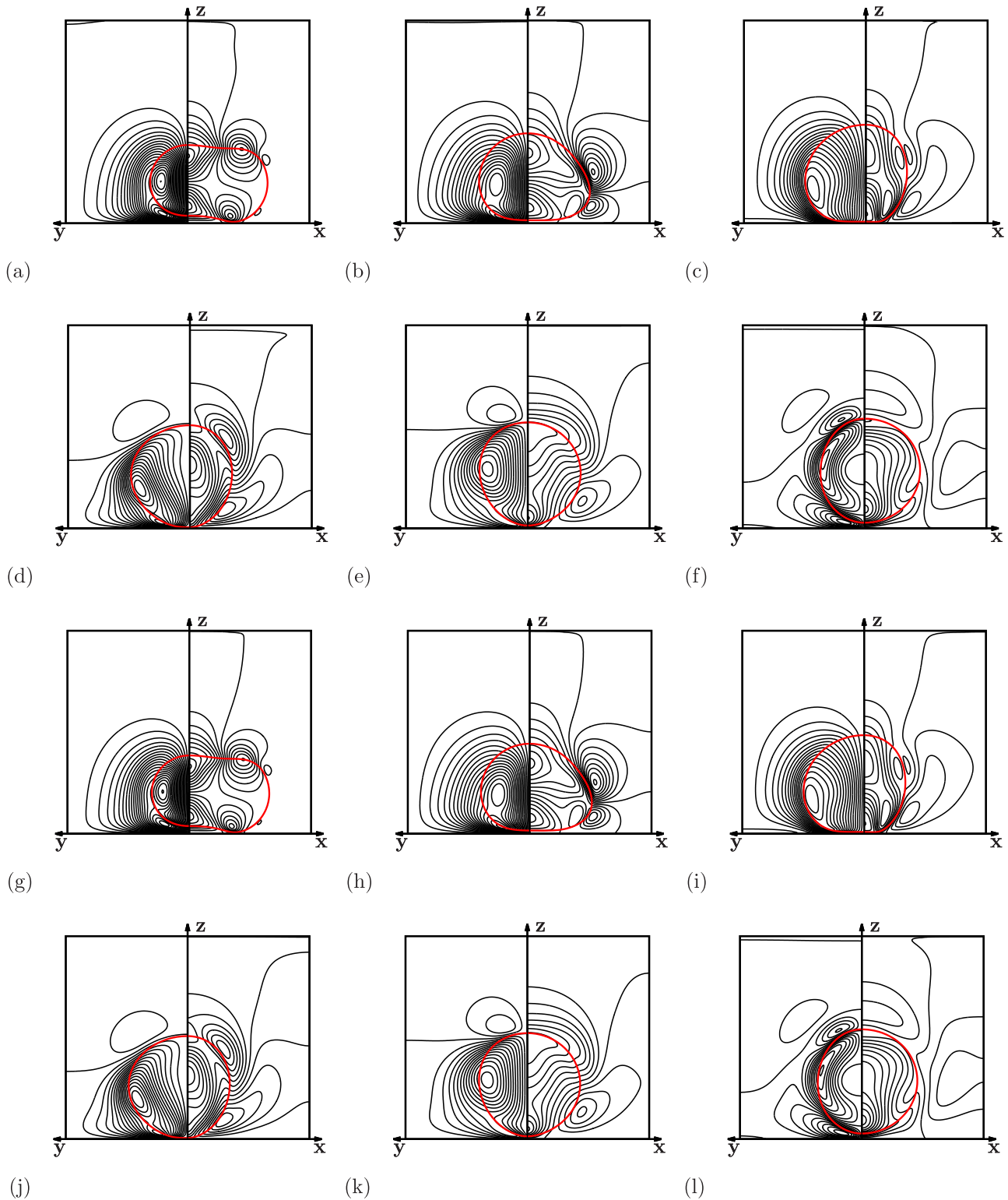


FIG. 22. Snapshots of the drop shapes (in red solid lines) and the contour plots of the velocity component  $w$  in the middle  $y$ - $z$  and  $x$ - $z$  planes at  $t = 1.0, 2.0, 3.0, 4.0, 5.0,$  and  $6.0$  [(a)–(f) by the present SMAMEs simulation and (g)–(l) by the 3D MRT-LBM simulation] at  $Oh = 0.037$  for the coalescence induced drop jumping on a nonwetting wall. In each panel, the left part shows the middle  $y$ - $z$  plane at  $x = 0$  and the right shows the middle  $x$ - $z$  plane at  $y = 0$ . The shared simulation parameters are as in Fig. 20.

Because the two fluids have the same density and viscosity, they are better viewed as two liquid phases. Under such conditions, the coalesced drop experiences larger drag forces and gains less momentum to jump than water drops in air (as in

the experiments [48]). On the other hand, it was reported that coalescence induced drop jumping can also occur when the ambient fluid is another liquid [49] (if it is on a hydrophobic fiber and the viscosity is moderate). Here our main purpose

is not to investigate the physical problem in detail. We only intend to simulate typical cases of this interesting problem by using the proposed method to evaluate its accuracy and efficiency.

For this problem, the capillary-inertial velocity and time,  $U_{ci} = \sqrt{\sigma/(\rho_0 R)}$  and  $T_{ci} = L_c/U_{ci}$ , are used to scale the velocity and time quantities. Two cases at  $Oh = 0.037$  ( $Re = 730.46$ ) and  $Oh = 0.119$  ( $Re = 70.616$ ) were simulated. Figure 20 shows the evolutions of the centroid velocity of the drop in the  $z$  direction  $W_{\text{drop}}$  computed by the present method and by the 3D LBM (same as that in Sec. III G) using the same numerical parameters ( $N_L = 40$ ,  $c = 10$ ,  $Cn = 0.1$ ,  $Pe = 8 \times 10^3$ ). The grid size is  $120 \times 120 \times 200$ . It can be found that the present results are in very good agreement with the LBM results for both  $Oh = 0.037$  and  $0.119$ . In addition, to illustrate the coalescence and jumping process at  $Oh = 0.037$  and to better gauge the quality of simulation, we also examined the interfaces and the velocity components  $u$ ,  $v$  and  $w$  in two planes of symmetry at several selected times. Figure 21 shows the drop shapes and the contour plots of the velocity component  $u$  (in the middle  $x$ - $z$  plane) and  $v$  (in the middle  $y$ - $z$  plane) at  $t = 1.0, 2.0, 3.0, 4.0, 5.0$ , and  $6.0$  for the case at  $Oh = 0.037$ . Besides, Fig. 22 gives the contour plots of the velocity component  $w$  in these two planes at the same times. It was found that the drop jumped off the wall after some time when  $Oh = 0.037$  (e.g., see the snapshots at  $t = 6.0$  in Fig. 21) and the drop always stayed on the wall when  $Oh = 0.119$  (not shown here). It is observed from Figs. 21 and 22 that both the drop shapes and the velocity contours by the present method resemble the LBM results to a large extent. This indicates that the present SMAMEs simulation can reproduce not only the average quantities (e.g.,  $W_{\text{drop}}$ ) but also the interface and flow details reasonably close to the LBM for complex two-phase flow problems. It is noted that the simulation time using the present SMAMEs is much shorter than that using the LBM. For example, to run 40 steps using four computational nodes on the same computer, the present method takes about 26 s, whereas the LBM (D3Q19) takes about 70 s. Here the LBM is parallelized by the MPI with the domain decomposed into four parts in the  $x$  direction and the SMAMEs is implemented in the AMReX framework

[50] with its default domain decomposition method (the solution of the CHE is similar in both solvers). One can see that the present method is *nearly three times faster* than the LBM in the simulation of 3D two-phase flows. Note that the present method was also implemented using the same domain decomposition and parallelization as the LBM. In that case, it is about two times faster than the LBM for this 3D two-phase problem.

#### IV. CONCLUDING REMARKS

To summarize, inspired by the MAMEs and LBM, we have proposed a simplified numerical method to simulate incompressible viscous flows. It was verified through a number of tests of single-phase, thermal, and two-phase flows in 2D, axisymmetric, and 3D geometries. The results of all cases are as accurate as the LBM/MAMEs results and/or in good agreement with other reference results from analytical solutions or directly solving the incompressible NSEs. At the same time, its implementation is much easier and the simulations using this method cost much less memory and time than the corresponding LBM simulations. Some issues associated with the MAMEs, such as the use of intermediate variables and predictor-corrector step and the boundary conditions for additional derivatives, are no longer present in our method. Unlike the situation in the LBM, the inclusion of external forces is straightforward since the macroscopic governing equations are handled directly. For two-phase flows, a limitation of the present method is that it can only deal with flows with constant viscosity and density (at most, with small density ratios). In future, it will be further extended for flows with larger density and viscosity contrasts. That may require more in-depth analyses of the LBEs for such problems.

#### ACKNOWLEDGMENTS

This work is supported by the National Natural Science Foundation of China (NSFC, Grant No. 11972098). Constructive comments by the anonymous reviewers are highly appreciated.

- 
- [1] J. H. Ferziger and M. Peric, *Computational Methods for Fluid Dynamics* (Springer, New York, 1999).
  - [2] S. Chen and G. D. Doolen, *Annu. Rev. Fluid Mech.* **30**, 329 (1998).
  - [3] X. He, G. D. Doolen, and T. Clark, *J. Comput. Phys.* **179**, 439 (2002).
  - [4] T. Ohwada and P. Asinari, *J. Comput. Phys.* **229**, 1698 (2010).
  - [5] T. Ohwada, P. Asinari, and D. Yabusaki, *Comput. Math. Appl.* **61**, 3461 (2011).
  - [6] M. Junk and A. Klar, *SIAM J. Sci. Comput.* **22**, 1 (2000).
  - [7] M. Junk, *Numer. Methods Partial Differ. Eq.* **17**, 383 (2001).
  - [8] J. Lu, H. Lei, C. Shu, and C. Dai, *J. Comput. Phys.* **415**, 109546 (2020).
  - [9] S. Ansumali, I. V. Karlin, and H. C. Ottinger, *Phys. Rev. Lett.* **94**, 080602 (2005).
  - [10] I. V. Karlin, A. G. Tomboulides, C. E. Frouzakis, and S. Ansumali, *Phys. Rev. E* **74**, 035702(R) (2006).
  - [11] S. Borok, S. Ansumali, and I. V. Karlin, *Phys. Rev. E* **76**, 066704 (2007).
  - [12] A. Toutant, *J. Comput. Phys.* **374**, 822 (2018).
  - [13] P. Asinari, T. Ohwada, E. Chiavazzo, and A. F. D. Rienzo, *J. Comput. Phys.* **231**, 5109 (2012).
  - [14] J. R. Clausen, *Phys. Rev. E* **87**, 013309 (2013).
  - [15] Y. T. Delorme, K. Puri, J. Nordstrom, V. Linders, S. Dong, and S. H. Frankel, *Comput. Fluids* **150**, 84 (2017).
  - [16] A. Kajzer and J. Pozorski, *Comput. Math. Appl.* **76**, 997 (2018).
  - [17] X. Shi and C. Lin, *Flow, Turbul. Combust.* **105**, 67 (2020).

- [18] D. Dupuy, A. Toutant, and F. Bataille, *J. Comput. Phys.* **411**, 109407 (2020).
- [19] A. Toutant, *Phys. Lett. A* **381**, 3739 (2017).
- [20] P. J. Dellar, *Phys. Rev. E* **64**, 031203 (2001).
- [21] M. Hortmann, M. Peric, and G. Scheuerer, *Int. J. Numer. Meth. Fluids* **11**, 189 (1990).
- [22] Z. Guo, B. Shi, and C. Zheng, *Int. J. Numer. Meth. Fluids* **39**, 325 (2002).
- [23] Y. Peng, C. Shu, and Y. T. Chew, *Phys. Rev. E* **68**, 026701 (2003).
- [24] D. Jacqmin, *J. Comput. Phys.* **155**, 96 (1999).
- [25] J. J. Huang, C. Shu, and Y. T. Chew, *Int. J. Numer. Meth. Fluids* **60**, 203 (2009).
- [26] J. W. Cahn and J. E. Hilliard, *J. Chem. Phys.* **28**, 258 (1958).
- [27] J.-J. Huang, H. Huang, and X. Wang, *Int. J. Numer. Meth. Fluids* **77**, 123 (2015).
- [28] J.-J. Huang, H. Huang, C. Shu, Y. T. Chew, and S.-L. Wang, *J. Phys. A: Math. Theor.* **46**, 055501 (2013).
- [29] A. Jameson, W. Schmidt, and E. Turkel, in *Proceedings of the 14th Fluid and Plasma Dynamic Conference, Palo Alto, California, June 23–25, 1981* (AIAA, Reston, VA, 1981), paper AIAA 1981-1259.
- [30] V. Esfahanian and P. Akbarzadeh, *Appl. Math. Comput.* **206**, 651 (2008).
- [31] P. Lallemand and L.-S. Luo, *Phys. Rev. E* **61**, 6546 (2000).
- [32] A. Fakhari, D. Bolster, and L.-S. Luo, *J. Comput. Phys.* **341**, 22 (2017).
- [33] D. J. Holdych, D. R. Noble, J. G. Georgiadis, and R. O. Buckius, *J. Comput. Phys.* **193**, 595 (2004).
- [34] M. Junk, A. Klar, and L.-S. Luo, *J. Comput. Phys.* **210**, 676 (2005).
- [35] S. A. Orszag, in *Computing Methods in Applied Sciences and Engineering Part 2*, edited by R. Glowinski and J. L. Lions (Springer, Berlin, 1974), pp. 50–64.
- [36] M. E. Brachet, D. I. Meiron, S. A. Orszag, B. G. Nickel, R. H. Morf, and U. Frisch, *J. Fluid Mech.* **130**, 411 (1983).
- [37] N. Sharma and T. K. Sengupta, *Phys. Fluids* **31**, 035106 (2019).
- [38] U. Ghia, K. N. Ghia, and C. T. Shin, *J. Comput. Phys.* **48**, 387 (1982).
- [39] C. Shu, X. D. Niu, and Y. T. Chew, *Int. J. Mod. Phys. C* **14**, 925 (2003).
- [40] S. Hou, Q. Zou, S. Chen, G. Doolen, and A. C. Cogley, *J. Comput. Phys.* **118**, 329 (1995).
- [41] M. L. Minion and D. L. Brown, *J. Comput. Phys.* **138**, 734 (1997).
- [42] G. D. V. Davis, *Int. J. Numer. Meth. Fluids* **3**, 249 (1983).
- [43] C. Shu and H. Xue, *Int. J. Heat Fluid Flow* **19**, 59 (1998).
- [44] A. Prosperetti, *Phys. Fluids* **24**, 1217 (1981).
- [45] J. Kim, *J. Comput. Phys.* **204**, 784 (2005).
- [46] J. Han and G. Tryggvason, *Phys. Fluids* **11**, 3650 (1999).
- [47] J.-J. Huang, H. Huang, and S.-L. Wang, *Prog. Comput. Fluid Dyn.* **15**, 26 (2015).
- [48] J. B. Boreyko and C.-H. Chen, *Phys. Rev. Lett.* **103**, 184501 (2009).
- [49] K. Zhang, F. Liu, A. J. Williams, X. Qu, J. J. Feng, and C.-H. Chen, *Phys. Rev. Lett.* **115**, 074502 (2015).
- [50] W. Zhang, A. Almgren, V. Beckner, J. Bell, J. Blaschke, C. Chan, M. Day, B. Friesen, K. Gott, D. Graves *et al.*, *J. Open Source Software* **4**, 1370 (2019).